The ESSENCE Supernova Survey: Survey Optimization, Observations, and Supernova Photometry — **Source link** ⌞↗⌟

G. Miknaitis, G. Pignata, Armin Rest, W. M. Wood-Vasey ...+36 more authors

Institutions: Fermilab, Pontifical Catholic University of Chile, Harvard University, Texas A&M University ...+12 more institutions

Topics: Photometry (astronomy), Light curve, Redshift and Dark energy

Related papers:

- Hubble Space Telescope Observations of Nine High-Redshift ESSENCE Supernovae

- Photometric Estimates of Redshifts and Distance Moduli for Type Ia Supernovae

- Photometric selection of Type Ia supernovae in the Supernova Legacy Survey

- A New Determination of the High Redshift Type Ia Supernova Rates with the Hubble Space Telescope Advanced Camera for Surveys

- A Model-independent Photometric Redshift Estimator for Type Ia Supernovae

THE ESSENCE SUPERNOVA SURVEY: SURVEY OPTIMIZATION, OBSERVATIONS, AND SUPERNOVA PHOTOMETRY

G. Miknaitis,[1] G. Pignata,[2] A. Rest,[3] W. M. Wood-Vasey,[4] S. Blondin,[4] P. Challis,[4] R. C. Smith,[3] C. W. Stubbs,[4,5]
N. B. Suntzeff,[3,6] R. J. Foley,[7] T. Matheson,[8] J. L. Tonry,[9] C. Aguilera,[3] J. W. Blackman,[10] A. C. Becker,[11]
A. Clocchiatti,[2] R. Covarrubias,[11] T. M. Davis,[12] A. V. Filippenko,[7] A. Garg,[4,5] P. M. Garnavich,[13]
M. Hicken,[4,5] S. Jha,[7,14] K. Krisciunas,[6,13] R. P. Kirshner,[4] B. Leibundgut,[15] W. Li,[7] A. Miceli,[11]
G. Narayan,[4,5] J. L. Prieto,[16] A. G. Riess,[17,18] M. E. Salvo,[10] B. P. Schmidt,[10]
J. Sollerman,[12,19] J. Spyromilio,[15] AND A. Zenteno[3]

ABSTRACT

We describe the implementation and optimization of the ESSENCE supernova survey, which we have undertaken to measure the dark energy equation-of-state parameter, $w = P/(\rho c^2)$. We present a method for optimizing the survey exposure times and cadence to maximize our sensitivity to w for a given fixed amount of telescope time. For our survey on the CTIO 4 m telescope, measuring the luminosity distances and redshifts for supernovae at modest redshifts ($z \approx 0.5 \pm 0.2$) is optimal for determining w. We describe the data analysis pipeline based on using reliable and robust image subtraction to find supernovae automatically and in nearly real time. Since making cosmological inferences with supernovae relies crucially on accurate measurement of their apparent brightnesses, we describe our efforts to establish a thorough calibration of the CTIO 4 m telescope's natural photometric system. In its first four years, ESSENCE has discovered and spectroscopically confirmed 102 Type Ia supernovae, at redshifts from 0.10 to 0.78, identified through an impartial, effective methodology for spectroscopic classification and redshift determination. We present the resulting light curves for all of the Type Ia supernovae found by ESSENCE and used in our measurement of w, presented in a companion paper by Wood-Vasey and coworkers.

Subject headings: cosmology: observations — methods: data analysis — supernovae: general — surveys

Online material: color figures

1. INTRODUCTION

This is a report on the first four years of the ESSENCE survey (Equation of State: SupErNovae trace Cosmic Expansion), a program to measure the dark energy equation-of-state parameter, $w = P/(\rho c^2)$ (where P is the pressure and ρ is the energy density), to a precision of 10% through the discovery and monitoring of high-

redshift Type Ia supernovae (SNe Ia). The motivations and goals of ESSENCE, as well as the methods and data, are presented here. ESSENCE is part of the exploration of the new and surprising picture of an accelerating universe, which has become the prevailing cosmological paradigm. This paradigm is supported by essentially all current observations, including those based on supernova distances, the large-scale clustering of matter, and fluctuations in the cosmic microwave background radiation. The free parameters of this concordance model can consistently fit these diverse and increasingly precise measurements.

This paper describes the survey design and optimization, as well as the acquisition and photometric analysis of our data through to the generation of photometrically calibrated SN light curves. The companion paper by Wood-Vasey et al. (2007) describes how luminosity distances are measured from the SN light curves and derives constraints on w from the ESSENCE observations.

1.1. Cosmology and Dark Energy

While the current observational agreement on a concordance model is surprisingly good (Tegmark et al. 2004; Eisenstein et al. 2005; Spergel et al. 2007), it comes at the high cost of introducing two unknown forms of mass energy: nonbaryonic cold dark matter (CDM), and dark energy that exerts negative pressure. Each is a radical idea, and it is only because multiple independent observations require their existence that we have come to seriously consider new physics to account for these astronomical phenomena.

The dark energy problem is currently one of the most challenging issues in the physical sciences. The stark difference between the staggeringly *large* value for the vacuum energy predicted by quantum field theory and the cosmic vacuum energy density inferred

[1] Fermi National Accelerator Laboratory, Batavia, IL 60510-0500; gm@fnal.gov.

[2] Pontificia Universidad Católica de Chile, Departamento de Astronomía y Astrofísica, Casilla 306, Santiago 22, Chile.

[3] Cerro Tololo Inter-American Observatory, National Optical Astronomy Observatory, Casilla 603, La Serena, Chile.

[4] Harvard-Smithsonian Center for Astrophysics, Cambridge, MA 02138.

[5] Department of Physics, Harvard University, Cambridge, MA 02138.

[6] Department of Physics, Texas A&M University, College Station, TX 77843-4242.

[7] Department of Astronomy, University of California, Berkeley, CA 94720-3411.

[8] National Optical Astronomy Observatory, Tucson, AZ 85719-4933.

[9] Institute for Astronomy, University of Hawaii, Honolulu, HI 96822.

[10] Research School of Astronomy and Astrophysics, Australian National University, Mount Stromlo and Siding Spring Observatories, Weston Creek PO 2611, Australia.

[11] Department of Astronomy, University of Washington, Seattle, WA 98195-1580.

[12] Dark Cosmology Centre, Niels Bohr Institute, University of Copenhagen, DK-2100 Copenhagen, Denmark.

[13] Department of Physics, University of Notre Dame, Notre Dame, IN 46556-5670.

[14] Kavli Institute for Particle Astrophysics and Cosmology, Stanford Linear Accelerator Center, MS 29, Menlo Park, CA 94025.

[15] European Southern Observatory, D-85748 Garching, Germany.

[16] Department of Astronomy, Ohio State University, Columbus, OH 43210.

[17] Space Telescope Science Institute, Baltimore, MD 21218.

[18] Johns Hopkins University, Baltimore, MD 21218.

[19] Department of Astronomy, Stockholm University, AlbaNova, 10691 Stockholm, Sweden.

from observations (e.g., Einstein's "cosmological constant," Λ) leads us to wonder how this vacuum energy of the universe could be so *small* (Weinberg 1989; Carroll et al. 1992; Padmanabhan 2003; Peebles & Ratra 2003). On the other hand, the convergence of observations that give rise to the ΛCDM concordance cosmology, with $\Omega_\Lambda \approx 0.7$ rather than identically zero, forces us to ask why the vacuum energy is so large.

More broadly, these cosmological observations can be interpreted as evidence for physics beyond our standard models of gravitation and quantum field theory. It is perhaps no coincidence that this occurs at the friction point between these two independently successful, but as yet unmerged, paradigms. Our understanding of the gravitational implications of quantum processes appears to be quite incomplete.

The dark energy problem challenges us on many fronts: theoretical, observational, and experimental. Observational cosmology has an important role to play, and the current challenge is to undertake measurements that will lead to a better understanding of the nature of the dark energy (Albrecht et al. 2006). In particular, we seek to measure the equation-of-state parameter, w, of the dark energy, as this can help us test theoretical models. One specific goal is to establish whether the observed accelerating expansion of the universe is due to a classical cosmological constant (Λ) or some other new physical process.

Within the framework of Friedmann-Robertson-Walker cosmology, the only way to reconcile the observed geometric flatness and the observed (and inferred) matter density is through another component of mass energy that does not clump with matter. The observation of acceleration from SNe Ia is the unique clue that indicates that this component must have negative pressure (Riess et al. 1998, 2001, 2004, 2007; Perlmutter et al. 1999; Tonry et al. 2003; Knop et al. 2003; Barris et al. 2004; Clocchiatti et al. 2006; Astier et al. 2006). As the evidence from SNe Ia has grown more conclusive, the focus has shifted from verifying the existence of dark energy to constraining its properties (Freedman & Turner 2003). Accordingly, several large-scale, multiyear supernova surveys have embarked on studying dark energy by collecting large, homogeneous data sets. The Supernova Legacy Survey (SNLS) has published cosmological constraints using 73 SNe Ia from its first-year sample (Astier et al. 2006) between redshifts z of 0.2 and 1.0, and it continues to accumulate data. More recently, the Sloan Digital Sky Survey II (SDSS-II) Supernova Survey (Frieman et al. 2004) has observed $\sim$200 SNe Ia at redshifts out to 0.4. The final SN Ia samples from each of these programs and ESSENCE will each number in the hundreds.

Of the various models for dark energy currently being discussed in the literature, the cosmological constant Λ (i.e., some uniform vacuum energy density) holds a special place, as both the oldest, originating with Einstein, and, in many ways, the simplest (Carroll et al. 1992). Quantum field theory suggests how to calculate the energy of the vacuum, but there is no plausible theoretical argument that accounts for the small, but nonzero, value required by observations. A host of other alternatives have been proposed (Copeland et al. 2006), many of which appeal to slowly rolling scalar fields, similar to those used to describe inflation. Such models readily produce predictions that agree with the current observational results, but they suffer from a lack of clear physical motivation, being concocted after the fact to solve a particular problem. Another class of ideas appeals to higher dimensional "brane world" physics inspired by string theory: for example, the cyclic universe (Steinhardt & Turok 2002; Steinhardt & Turok 2005), or modifications to gravity due to the existence of extra dimensions (Dvali et al. 2003).

One straightforward way to parameterize the dark energy is by assuming that its equation of state takes the form $P = w\rho c^2$,

where P and ρ are pressure and density, respectively, related by an "equation-of-state parameter" w. Nonrelativistic matter has $w = 0$, while radiation has $w = +\frac{1}{3}$, and different proposed explanations for the dark energy have a variety of values of w. In general, to produce an accelerated expansion, a candidate dark energy model must have $w < -\frac{1}{2}$ for a current matter density of $\Omega_M \approx \frac{1}{3}$. The classical cosmological constant, Λ, of the general theory of relativity has $w = -1$ exactly, at all times. Other models can take on a variety of effective w-values that may vary with time. For example, quintessence (e.g., Steinhardt 2003) posits a minimally coupled rolling scalar field, with

$$ w \approx \frac{P}{\rho} = \frac{(1/2)\dot{\phi}^2 - V(\phi)}{(1/2)\dot{\phi}^2 + V(\phi)}, \tag{1} $$

where we take $c = 1$. In this case, the effective value of w depends on the form of the potential chosen and can evolve with redshift. In general, the parameterization of dark energy in terms of w is a convenient and useful tool to compare a variety of models (Weller & Albrecht 2002).

As a first step toward determining the nature of dark energy, the obvious place to start is to test whether the observed value of w is consistent with -1 (Garnavich et al. 1998). If not, then a cosmological constant is ruled out as the explanation for dark energy.

If w is measured to be consistent with -1, then while models that exhibit an effective $w \approx -1$ are still allowed, the range in parameter space in which they can exist will be significantly restricted. Breaking the degeneracy between Λ and such "impostors" would then require measurements of the additional parameters that describe their time dependence. However, the form of such a parameterization is at present largely unrestricted and the choice of arbitrary parameterizations influences the conclusions derived from the analysis of the data (Upadhye et al. 2005). In the future, measurements of growth of large-scale structure, such as through weak-lensing surveys, will provide a powerful complement to SN Ia measurements in constraining the properties of dark energy, as well as checking for possible modifications to general relativity (Albrecht et al. 2006). In the short term, constraining w under the assumption that it is constant allows us to test a well-posed hypothesis that can be addressed with existing facilities and methods. Therefore, we restrict our considerations to w under the assumption that it is constant for the rest of this paper. While under standard general relativity w is bounded by the null dominant energy condition to be greater than or equal to -1, we should keep an open mind as to whether the data allow $w < -1$, since dark energy may well arise from physics beyond today's standard theories.

Motivated by these considerations, we have undertaken a project to use SNe Ia to measure w with a target fractional uncertainty of 10%. Observations of SNe Ia provided the first direct evidence for accelerating cosmic expansion (Riess et al. 1998; Perlmutter et al. 1999) and remain an incisive tool for studying the properties of the dark energy.

1.2. *Measuring the Physics of Dark Energy with Supernovae*

SNe Ia are among the most energetic stellar explosions in the universe. Their high peak luminosities ($\sim$$4 \times 10^9 L_\odot$) make SNe Ia visible across a large fraction of the observable universe. The peak luminosity can be calibrated to $\sim$15% precision in flux (Phillips 1993; Hamuy et al. 1996; Riess et al. 1996; Goldhaber et al. 2001; Guy et al. 2005; Jha et al. 2007). They are thus well suited to probing the expansion history during the epoch in which the universe has apparently undergone a transition from deceleration to

acceleration ($0 < z < 1$). The utility of SNe Ia as "standardizable" candles was established observationally by Phillips (1993) with the identification of a correlation between peak luminosity and width of the light curves.

The "Type Ia" designation is an observational distinction, denoting objects whose spectra lack hydrogen or helium features but exhibit a characteristic absorption trough observed at ~6150 Å, but attributed to Si II $\lambda 6355$ (for a review of supernova classification see Filippenko 1997). Following the original suggestion of Hoyle & Fowler (1960), these objects are now thought to almost certainly be the thermonuclear disruption of a carbon-oxygen white dwarf (C-O WD) at or near the Chandrasekhar mass limit (e.g., Woosley & Weaver 1986). Material gained through accretion from a companion star pushes the total mass of the C-O WD close to what can be supported by degeneracy pressure, resulting in a powerful nuclear burning wave that completely destroys the star. A large fraction of the progenitor fuses rapidly to produce ^{56}Ni, whose radioactive decay then powers the observed light curve (Colgate & McKee 1969). Bolometric light curves suggest that ~0.7 $M_\odot$ of ^{56}Ni is produced, implying that the burning is incomplete (Contardo et al. 2000; Stritzinger et al. 2006). There is disagreement on important details of whether the burning wave is purely subsonic (a deflagration) or partly supersonic (a detonation; Hillebrandt & Niemeyer 2000). Nevertheless, models for the explosion give broad agreement with the observed light curves and spectra, although the specifics of progenitors and explosion physics remain unresolved (Branch et al. 1995; Renzini 1996; Nomoto et al. 2000; Livio 2000).

Fortunately, thus far the lack of a detailed understanding of supernova physics has not prohibited the use of these objects as probes of cosmology; the empirical correlations of light-curve shape and color with luminosity appear to largely "standardize" SNe Ia. Subtle effects such as how SNe Ia are connected to stellar populations and how those populations may change with time (e.g., typical initial mass of the WD, chemical composition) will certainly become important in the future as we attempt to place ever tighter constraints on dark energy (Hamuy et al. 2000; Jha 2002; Gallagher et al. 2005; Sullivan et al. 2006). For example, observations suggest that the most luminous SNe Ia are found only in galaxies with current star formation.

As in classical physics, the flux density from a cosmological source falls off in proportion to the inverse square of distance,

$$\mathcal{F} = \frac{L}{4\pi D_l^2}. \tag{2}$$

However, this "luminosity distance," D_l, depends on how the universe expands as a photon travels from emitter to receiver, which in turn depends sensitively on the composition and properties of the constituents of the cosmic mass energy density. Specifically, for a flat universe the luminosity distance as a function of redshift, $D_l(z)$, is given by

$$D_l(z) = \frac{c(1+z)}{H_0}$$
$$\times \int_0^z \frac{1}{\sqrt{(1-\Omega_M)(1+z')^{3(1+w)} + \Omega_M(1+z')^3}}\, dz', \tag{3}$$

where w is taken here to be constant. In cosmological analyses, the combination of the Hubble constant and the intrinsic luminosity of SNe Ia is a multiplicative nuisance parameter that scales dis-
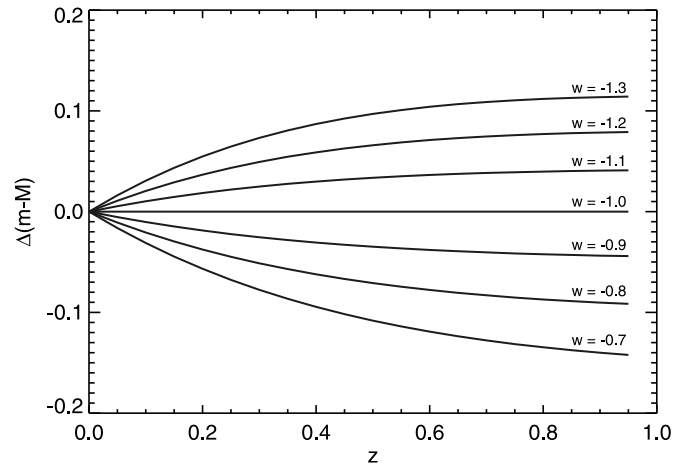

Fig. 1.—Differences in distance modulus, in units of magnitudes, for various values of w as a function of redshift, relative to $w = -1$, for $\Omega_M = 0.3$, $\Omega_\Lambda = 0.7$. Note that even at modest redshifts there is a significant fraction of the total asymptotic signal available. [*See the electronic edition of the Journal for a color version of this figure.*]

tance measurements at all redshifts by the same amount. Thus, under the assumption of flatness ($\Omega_M + \Omega_X = 1$, where "X" denotes any energy component other than Ω_M), the only other free cosmological parameter when measuring w is the matter density, Ω_M.

If we seek to constrain w using the observed luminosity distance versus redshift relation, it is worth considering which redshifts are most incisive. The relative differences in distance modulus as a function of redshift, for different values of w, are shown in Figure 1, where Ω_M and Ω_Λ have been fixed at 0.3 and 0.7, respectively. There is a significant w-dependent signal even at intermediate redshifts ($z \approx 0.4$), where observations with a 4 m class telescope can readily yield many supernovae each month. Of course, observations such as the ESSENCE survey actually produce a complex set of constraints in cosmological parameter space, but much of the signal of interest is readily accessible at intermediate redshifts, between 0.3 and 0.8.

1.3. Considerations for Optimally Constraining w with SN Ia Observations

For a ground-based survey, a variety of factors determine the number of useful supernovae monitored and the uncertainties associated with each data point on the light curve. The overall quality of each supernova light curve, in turn, determines the precision of its luminosity distance. Some of the factors that impact the ability of a particular survey strategy to constrain cosmological parameters are as follows:

1. Typical site conditions: seeing, weather, sky background, atmospheric transmission.
2. System throughput versus wavelength: aperture, optics, field of view, detector quantum efficiency.
3. Temporal constraints: telescope scheduling constraints, camera readout time.
4. Data quality: requisite signal-to-noise ratio (S/N) and cadence required for distance determination.
5. Passbands: number of different bands needed for extinction and SN color discrimination.
6. Spectroscopic considerations: location, availability, and scheduling of follow-up spectroscopic resources.

In order to optimize the observational survey strategy for ESSENCE, we tried to parameterize several of the factors above

and balance them to obtain the strongest constraints on w. With the prominent cosmological signal available in the redshift range from 0.3 to 0.8, it is clear that a wide-field camera on a 4 m class telescope can provide the needed balance of photometric depth (at $z = 0.5$, SNe Ia have $m \approx 22$ mag at peak) and sky coverage. Smaller fields of view on larger telescopes are better suited to going to higher redshifts, while wider fields on smaller telescopes are only able to reach redshifts where the cosmological signal is small. Combining these criteria with the range of spectroscopic follow-up facilities available to our collaboration, we focused our analysis on the Blanco 4 m telescope at the Cerro Tololo Inter-American Observatory (CTIO) together with the MOSAIC camera as providing an optimal combination of site (seeing plus weather), aperture, field of view, and telescope scheduling.

Beyond the selection of appropriate telescopes and instrumentation, there are relatively few "free parameters" controllable by the observers. These include the optical passbands used, the exposure time in each passband for each field, the total number of fields monitored, the cadence of the repeated observations, and the ability to obtain spectra for each supernova candidate.

The calibration of SN Ia luminosity from light-curve shape is currently best understood in the rest-frame B and V passbands. These passbands map to observer-frame R and I for SNe Ia at $z \approx 0.4$ (i.e., the uncertainties in K-corrections [Nugent et al. 2002] are small). SN Ia $B - V$ color has been shown to span 0–1 mag at peak (as a function of the luminosity parameter), evolving to a much more uniform $B - V$ color of ~1 mag at 35 days after maximum brightness (Riess et al. 1996). Therefore, observations taken in the R and I passbands, with the I-band exposure time equal to twice that of R (therefore, ~0.75 mag deeper in I for similar detector quantum efficiency and sky background), are sufficient to roughly match the survey depth in both bands.

While observations in a third bandpass would aid in determination of color, and thus improve the estimates of extinction in the host galaxies, such observations would require significant additional observing time and are not easily accommodated within our optimization of limited observing time, photometric depth, sky coverage, and number of resulting SNe. Acquiring V-band observations would provide a better match to rest-frame B for low-redshift objects, but SNe in our sample should be bright and have well-measured colors at these redshifts. Observations in the z band would aid the color determination at higher redshifts, but the low quantum efficiency of the MOSAIC CCD detectors, as well as the brightness of the night sky in this band and the heavy fringing due to night-sky emission lines, makes obtaining useful data in this band impractical.

Therefore, by limiting our strategy to R and I and demanding that the I-band exposure times scale with the R-band exposure times, the survey optimization problem is then reduced to considering a single free parameter: the distribution of R-band integration times across the survey fields for a given fixed amount of telescope time. What is the balance between survey depth (which extends the redshifts probed) and area (which increases the area covered by each redshift slice)?

Consider the cosmological information contained in a single, perfect measurement of distance and redshift. Under the assumption of flat global geometry (and with perfect knowledge of H_0 and the intrinsic luminosity of SNe Ia), each such measurement traces out a curve of allowable values of Ω_M and w, as shown in Figure 2. It is clear that if the goal is to measure w from SNe Ia alone, a large span in redshift is desirable in order to maximize the orthogonality of the curves and break the degeneracy between matter density and the equation-of-state parameter.
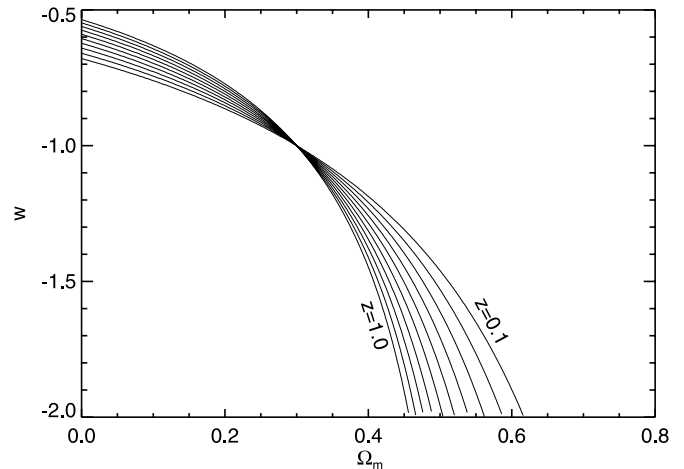

Fig. 2.—Curves in Ω_M and w for perfect measurements of distance at redshifts from 0.1 to 1.0, in steps of $\Delta z = 0.1$, for $\Omega_M = 0.3$, $\Omega_\Lambda = 0.7$.

However, since the difference between these curves is small even over a large span in redshift, such a measurement would require massive numbers of SNe Ia achievable only by next-generation experiments, such as DES, Pan-STARRS, LSST, or JDEM. In the short term, we may appeal to other cosmological measurements to provide a constraint on Ω_M, such as from large-scale structure measurements. This affords us some freedom in the redshifts at which we make our measurements, since the constraints from distance measurements are nearly orthogonal to an Ω_M prior of ~0.3 at all redshifts.[20] Although the sensitivity to differences in cosmological models is weaker at lower redshifts, there is a powerful observational advantage to working there because obtaining good photometric and spectroscopic measurements is far cheaper in units of telescope time.

To understand the trade-offs between the cosmological sensitivity of samples obtainable under different observational strategies, we carry out simulations to predict the number, as well as the distribution in redshift and magnitude, of the set of SNe Ia detectable in a survey of a given length and limiting magnitude set by the R-band exposure time. We adopt the methodology used by Tonry et al. (2003) to model the redshift-magnitude distribution of SNe Ia. In brief, we assume the SN Ia luminosity function used by Li et al. (2001a) modeled as three distinct luminosity classes representing "normal," overluminous (SN 1991T–like; e.g., Filippenko et al. 1992b), and subluminous (SN 1991bg–like; e.g., Filippenko et al. 1992a) SNe Ia, each following a Gaussian distribution. This is then convolved with an estimated distribution of extinction due to dust in the supernova host galaxies (Hatano et al. 1998). We can then generate mock SN Ia samples for various possible survey implementations. For the purposes of survey optimization, it is sufficient to restrict our considerations to flat cosmologies, neglecting degeneracies with Ω_{total}.

To estimate the achievable cosmological constraints, we use an analytic description of how the uncertainty in distance modulus depends on redshift, as the typical S/N of the photometry decreases at higher redshift, but the temporal sampling (in the

---

[20] We consider here a prior on Ω_M alone, but in reality constraints from measurements of the matter power spectrum, baryon acoustic oscillations, or the cosmic microwave background produce constraints that have at least mild degeneracy with other cosmological parameters. This simple prior is sufficient for the survey optimization arguments presented here.
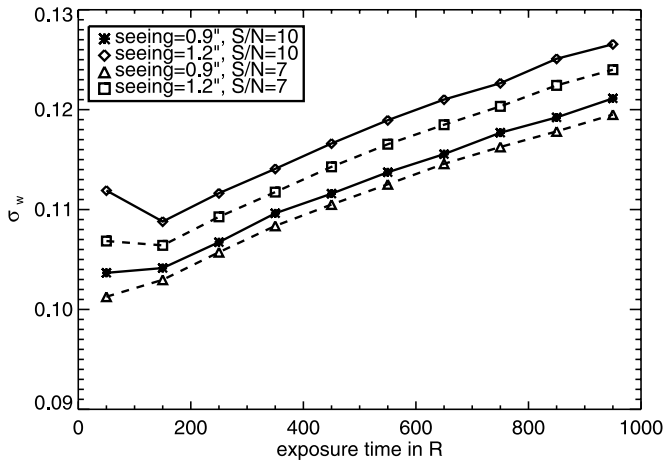
Fig. 3.—Estimated final uncertainty in w for a five-year ESSENCE survey when combined with a Gaussian prior on Ω_M centered on 0.3 and having a width of $\sigma = 0.04$ (Tegmark et al. 2004), as a function of R-band exposure time for the survey. A range of typical survey seeing conditions and detection thresholds was chosen. Here we show the effects of mean seeing, which degrades the precision of the photometry, and the S/N threshold at which we are able to detect SNe Ia in our data, which affects the total number of SNe observable.

SN rest frame) improves due to time dilation. The uncertainty in distance modulus is approximated by the expression

$$\delta_\mu(z) = \frac{1.3}{(S/N)_{peak}} \sqrt{\frac{\Delta t_{obs}}{1+z}} \sqrt{\frac{N_{obs}}{N_{obs} - 3}}, \qquad (4)$$

where Δt_{obs} gives the time in days between observations, N_{obs} specifies the number of observations between -10 and $+15$ days (relative to maximum) in the SN rest frame, and the $N_{obs} - 3$ term arises from 3 degrees of freedom in the fit of an SN light-curve time of maximum, luminosity at maximum, and width of the light curve.

This contribution to the distance uncertainty due to observational constraints is then summed in quadrature with the intrinsic dispersion in SN Ia peak luminosities, taken conservatively to be 0.2 mag. With the resulting mock Hubble diagrams, we then can predict the cosmological constraints obtainable for a given survey depth.

1.4. The ESSENCE Strategy

This generalized analysis can now be applied to our selected observational system, the Blanco 4 m telescope, in order to derive an optimal balance of photometric depth (or, equivalently, exposure time) and sky coverage given the range of conditions one might expect during a survey using a fixed amount of observing time. During the first year, we had used a mixture of exposure times, in order to achieve a broader redshift distribution, and we wished to reconsider the optimal strategy for our program. We assumed a five-year survey with ~15 nights per year spread over 3 months each year. The results are shown in Figure 3. We find that the final achievable uncertainty in w is surprisingly insensitive to the survey depth, with the trade-off between the number of SNe and the redshifts at which they are found roughly canceling. There is a weak optimum at $t_R = 200$ s because very shallow surveys lose cosmological leverage as the probed redshift range decreases. Following this analysis, we adopted exposure times of $t_R = 200$ s and $t_I = 400$ s beginning in the second year of the survey.

In optimizing the survey, we did not include systematic uncertainties in our model, as it is difficult to estimate the magni-

tude or form of these effects prior to carrying out the survey. Indeed, one of the goals of the ESSENCE survey is a hard quantification of these sources of systematic error. Given that we did not know an appropriate systematic error model and that an incorrect one might drive the optimization to a different conclusion, we have chosen to ignore systematic errors for the purpose of survey optimization. An additional advance of carrying out a shallower survey is that spectroscopic follow-up observations are far less expensive for lower redshift targets.

2. THE ESSENCE SURVEY

2.1. Observations

Based on the survey strategy described above, the ESSENCE team submitted a proposal to the National Optical Astronomy Observatory (NOAO) Survey program in 2002. We chose to propose a survey strategy to share time with the ongoing SuperMACHO survey, which uses only half-nights on the Blanco 4 m telescope. ESSENCE was awarded 30 half-nights per year for a five-year program (recently extended to six years), as well as additional calibration time on the CTIO 0.9 m telescope together with some follow-up time on the WIYN 3.5 m telescope. The ESSENCE survey is generally scheduled during dark and gray time for 3 consecutive months, from October through December each year, although the timing of New Moons sometimes moves the schedule into September or January. Each month, we observe every other night over a span of 20 days centered on New Moon. This schedule leaves approximately 10 bright nights each month with no light-curve coverage.

2.1.1. The Instrument

ESSENCE survey data are taken using the MOSAIC II imaging camera, which consists of eight 2048×4096 pixel charge-coupled devices (CCDs) arranged in two rows of four, with gaps corresponding to ~50 pixels between rows and 35 pixels between columns. In the f/2.87 beam at prime focus, this yields a field of view of $0.6°$ on a side for a total area of 0.36 deg^2 on the sky. The CCDs are thinned, back-illuminated, silicon devices manufactured by SITe with 15 μm pixels. At the center of the focal plane, each pixel subtends $0.27''$ on a side, although the pixel scale varies quadratically as a function of radius due to optical aberrations, such that pixels at the corners of the camera subtend a smaller area on the sky by 8%.

The CCDs are read out in dual-channel mode, in which the chip is bisected in the long direction and read out in parallel through two separate amplifiers, for a total read time of about 100 s. Because the amplifiers are not perfectly identical, we treat the 16 resulting 1048×4096 "amplifier images" as independent data units in our data reduction process. All ESSENCE observations are taken through the Atmospheric Dispersion Corrector (ADC), which is composed of two independently rotating prisms that compensate for variation in atmospheric refraction with air mass.

2.1.2. ESSENCE Fields

We selected fields that are equatorial, so that they can be accessed by telescopes in the northern and southern hemisphere for follow-up spectroscopy. The fields are spaced across the sky so that all observations may be taken at low air mass. We chose regions with low Milky Way extinction, for maximum visibility of these faint extragalactic sources and to minimize systematic errors incurred by correcting for extinction due to the Milky Way. Fields with contamination from bright stars, whose large footprint in the imaging data would reduce the effective search area, were avoided. Additional considerations in field selection included a

TABLE 1
COORDINATES OF THE CENTERS OF THE ESSENCE SEARCH FIELDS

Field Name	R.A. (J2000.0)	Decl. (J2000.0)
waa1	23 29 52.92	−08 38 59.7
waa2	23 27 27.02	−08 38 59.7
waa3	23 25 01.12	−08 38 59.7
waa5	23 27 27.02	−09 14 59.7
waa6	23 25 01.12	−09 14 59.7
waa7	23 30 01.20	−09 44 55.9
waa8	23 27 27.02	−09 50 59.7
waa9	23 25 01.12	−09 50 59.7
wbb1	01 14 24.46	00 51 42.9
wbb3	01 09 36.40	00 46 43.3
wbb4	01 14 24.46	00 15 42.9
wbb5	01 12 00.46	00 15 42.9
wbb6	01 09 00.16	+00 10 43.3
wbb7	01 14 24.46	−00 20 17.1
wbb8	01 12 00.46	−00 20 17.1
wbb9	01 09 36.40	−00 25 16.7
wcc1	02 10 00.90	−03 45 00.0
wcc2	02 07 40.60	−03 45 00.0
wcc3	02 05 20.30	−03 45 00.0
wcc4	02 10 01.20	−04 20 00.0
wcc5	02 07 40.80	−04 20 00.0
wcc7	02 10 01.55	−04 55 00.0
wcc8	02 07 41.03	−04 55 00.0
wcc9	02 05 20.52	−04 55 00.0
wdd2	02 31 00.25	−07 48 17.3
wdd3	02 28 36.25	−07 48 17.3
wdd4	02 34 30.35	−08 19 18.2
wdd5	02 31 00.25	−08 24 17.3
wdd6	02 28 36.25	−08 24 17.3
wdd7	02 33 24.25	−08 55 18.2
wdd8	02 31 00.25	−09 00 17.3
wdd9	02 28 36.25	−09 00 17.3

NOTES.—Units of right ascension are hours, minutes, and seconds, and units of declination are degrees, arcminutes, and arcseconds. For reference, the CTIO 4 m MOSAIC II detector has a field of view of 0.36 deg^2.

TABLE 2
SUMMARY OF THE SUPERNOVA YIELDS FROM THE FIRST
FOUR YEARS OF ESSENCE OBSERVATIONS

Year	Spectroscopically Confirmed Supernovae	Type Ia Supernovae
2002	15	15
2003	37	33
2004	41	26
2005	46	28

curves. The complete analysis of the 2002 data will take place after these reference images are obtained. We provide summary information about the 15 spectroscopically confirmed SNe Ia from this season in Table 3, but we only present the light curves for four of these objects for which current reductions are of sufficient quality to merit use in the cosmological analysis of Wood-Vasey et al. (2007). The final ESSENCE supernova sample will include all of the 2002 objects.

Observations for the second year of ESSENCE began on 2003 September 29. In order to facilitate scheduling of follow-up observations with the *Hubble Space Telescope* (*HST*), which requires advance knowledge of the approximate location of the targets, it was necessary to cluster the search fields together into four groups. The new field set consisted of 32 fields, clustered spatially in sets of eight, such that they were within the pointing error box of *HST*. To the extent possible, fields from 2002 were used as the basis for the new fields. The fields were again divided into two separate sets, observed on alternating nights, providing an observational cadence of every four nights for any given field. In Table 1 we list the coordinates of the 32 search fields monitored by ESSENCE from 2003 onward. Results from the subset of nine ESSENCE supernovae observed with *HST* were presented in Krisciunas et al. (2005).

Weather and observing conditions in 2003 were greatly improved over 2002, although still somewhat substandard for typical conditions at Cerro Tololo. Unfortunately, one of the MOSAIC CCDs (containing amplifiers 5 and 6) failed shortly before the observations began, resulting in a 12.5% loss in efficiency. The failed CCD was replaced before our 2004 observing season, allowing us to recover the lost efficiency from then on. For the third and fourth years of ESSENCE, we maintained the same set of fields as in 2003 and the MOSAIC imager was stable. The supernova yields for each of the four years of the survey are summarized in Table 2. The ESSENCE search is successful and our program finds roughly twice as many objects with SN-like light curves than we can confirm spectroscopically each year.

2.2. *Image Analysis Pipeline*

The automated analysis of ground-based imaging data is a complicated multistage procedure, involving the removal of instrumental artifacts, detailed calibration of the data, and measurements of fluxes from the objects of interest. The particular requirements of the ESSENCE program are even more demanding, with additional constraints on time and optimal processing.

First, the objects of interest are transient and appear in the data masked by the background flux from their host galaxy. Past experience has shown that the most reliable way to find these objects is via image subtraction (e.g., Norgaard-Nielsen et al. 1989; Perlmutter et al. 1995; Schmidt et al. 1998). For each new image, an archival "template" frame from a previous epoch is subtracted pixel by pixel to remove constant sources, such as galaxies, to reveal the supernova candidates. Image subtraction software is not

preference for areas with minimal infrared cirrus (based on *IRAS* maps), a preference for areas out of both the Galactic and ecliptic planes, and a preference for fields that overlapped previous wide-field surveys such as the SDSS, the NOAO Deep Wide-Field Survey, and the Deep Lens Survey.

The first ESSENCE observations commenced on 2002 September 29 (UT dates are used throughout this paper). For this first year of operations, a set of 36 fields was defined. These fields were divided into two sets, which were then observed every other ESSENCE night, resulting in a cadence of every 4 nights on any particular field. This proved to be a challenging inaugural season for the project. The El Niño Pacific weather pattern was in effect, producing heavy cloud cover much of the time and resulting in either lost observing time or data of such poor quality that the detection of faint SNe was often not possible. Also, the newly commissioned computing cluster experienced catastrophic failure shortly after data collection began, bringing real-time analysis of the data to a standstill for much of that observing campaign. On November 10, the *I*-band filter sustained significant damage, resulting in a crack. This severely degraded the *I*-band data quality in CCDs 1 and 2 (amplifiers 1–4), resulting in a diminished effective field of view for the rest of the season. This filter was replaced on 2003 May 25.

As described below, many of the 2002 fields have not yet been repeated to provide template images to extract the SN Ia light

part of standard analysis packages, and we have invested significant effort in developing robust and reliable methods necessary for our project.

Second, supernovae must be detected in *real time*. While it is a part of our search strategy to revisit each field and build up a time series of photometric measurements of all objects, we rely on follow-up spectroscopic observations to verify the identity of candidate transients as SNe Ia and to establish their redshifts. Because SNe Ia at the distances that give cosmological leverage are faint ($m \approx 22$) even at maximum light, it is preferable to observe them near maximum light. SNe Ia rise to maximum light roughly 20 days after explosion in their rest frame (Riess et al. 1999b; Conley et al. 2006; Garg et al. 2007), and while time dilation stretches the rise time of a supernova by a factor of $1 + z$, a prompt detection allows us to schedule the spectroscopic observations into the available time. This real-time component adds a significant demand on the analysis of the survey data: the data must be processed automatically and reliably, in bulk, each night of the survey. In order to achieve the necessary real-time analysis, the ESSENCE images are transferred from the mountain to La Serena immediately after readout, so that processing can begin and alerts can be generated within minutes or hours of the observations.

Finally, supernovae are rare events. We expect roughly one SN Ia per MOSAIC field per month. Each MOSAIC field consists of $4096 \times 2048 \times 8 = 67{,}000{,}000$ pixels, and we must be able to reliably determine the roughly dozen pixels among those that contain signal, often only marginally above background noise, from a bona fide SN Ia.

We have developed a data pipeline that meets these demands, accepting raw images directly from the telescope and automatically producing lists of candidate objects only hours later. Floating point operations are carried out by a variety of programs, either drawn from publicly available astronomical software packages such as IRAF[21] or written by us (generally in the C language). These are tied together by a suite of Perl scripts, which handle process management and bookkeeping. Functionally, there are two separate pipelines. The first of these (`mscpipe`) performs tasks relevant for full MOSAIC images, and as output divides each single MOSAIC field into 16 1K × 4K pixel images corresponding to each CCD amplifier. From this point onward, the "amplifier images" are processed through `photpipe` and each amplifier is effectively treated as an independent detector. We refer to a single MOSAIC exposure as a MOSAIC field and the subdivided images as subfields. Below we provide a brief description of the data processing, focusing in particular on those stages that alter the data in ways significant for the analysis.

2.2.1. *Cross Talk Correction and Masking*

Pairs of CCDs in the MOSAIC II imager are read out through single electronics controllers, which, for some combinations of CCDs, results in low-level cross talk between the signals from different chips. The resulting effect is the appearance of "ghosts" in one subfield of bright objects appearing in another subfield. Fortunately, this effect is small in magnitude, on the order of 0.1%, and deterministic. The first stage of the `mscpipe` pipeline uses the most recent values of these cross talk coefficients measured by the observatory staff and subtracts these electronic artifacts from the affected portions of the MOSAIC field, using the `xtalk` task from the `mscred` package for IRAF.

We identify bad columns and pixels, as well as saturated pixels, and save them in a mask file. This mask file also contains the locations of diffraction spikes and a large aperture mask at the positions of very bright stars. The mask is propagated through the pipeline to the difference images, which allows us to keep track of any pixel that is even slightly contaminated by a masked pixel. Cross talk ghosts are not masked because the initial ghosting signal is of low amplitude, so any error in the correction is very small.

2.2.2. *Astrometric Calibration*

The transformation from pixel to sky coordinates is dominated by distortions caused by the optical system of the telescope that change only slightly over long periods of time and generally take the form of a polynomial in radius. Once the terms of this distortion function are known, the astrometric calibration of any particular image reduces to determining accurately the center of the distortion in that field, essentially an offset in x and y and a rotation. This is accomplished via the IRAF task `msccmatch` from the `mscred` package, which matches objects in the image to an existing catalog of the field with precise astrometry. The current standard for astrometry is the USNO CCD Astrograph Catalog 2 (UCAC; Zacharias et al. 2004), which covers all fields observed by ESSENCE. However, since ESSENCE is a significantly deeper survey, the SDSS (York et al. 2000) provides a better photometric overlap. We use the SDSS (which itself is tied to UCAC) in the fields for which SDSS has imaging data (∼73% of ESSENCE fields) and default to UCAC when there are no SDSS data.

When the supernovae are faint, their location in an image is poorly constrained, and we must rely on the astrometric solution to tell us precisely where to measure the flux. Errors in positioning the point-spread function (PSF) produce an underestimate of the object's flux. Therefore, accurate *relative* astrometric calibration is essential to measuring supernova flux at low S/N, since what matters is that we are able to map pixels from individual images to some consistent coordinate system. To this end, we generate astrometric catalogs from our own data, which are themselves calibrated to either SDSS or UCAC. All subsequent ESSENCE images are then registered to these internally generated catalogs.

The astrometric solution is also used to "warp" each image to a common pixel coordinate system, so that reference images can be subtracted from them. This is accomplished using the SWarp (Bertin et al. 2002) software package, using a Lanczos windowed sinc function to resample the pixels onto the new coordinate system.

2.2.3. *Flat-fielding*

In order to obtain consistent flux measurements across the plane of the MOSAIC imager, we must normalize the response of all the pixels. This flat-fielding is achieved in three steps. First, at the beginning of each night, a screen inside the telescope dome is illuminated and observed with the MOSAIC. These high-S/N flat fields enable us to accurately correct for pixel-to-pixel variations and other imperfections in the optical system but introduce large-scale variations (e.g., gradients due to nonuniform illumination of the flat-field screen). The second step is to combine all of the data from a night's observations. By masking all astronomical sources and combining with a median statistic, an image of the illumination of the focal plane due to the night sky is created. This "illumination correction" is also applied to the data, removing gradients of ∼1% across a CCD. Finally, we use the average difference in sky level between each CCD to further regularize the overall flux scaling, a 1% correction to the dome flats.

2.2.4. Photometric Calibration

Flat-fielded and SWarped images are then analyzed with the DoPHOT photometry package (Schechter et al. 1993) to identify and measure sources. The standard PSF photometry routines from DoPHOT are used to determine the best-fitting PSF for an image, summarized briefly here and described more fully by Schechter et al. (1993). DoPHOT begins by detecting objects by searching for clusters of pixels that are significantly above the background noise in the image. Beginning with the brightest objects, it classifies them and fits those that appear to be stellar with a PSF, determining the best-fitting model parameters for the set of objects. The DoPHOT PSF model is of the form

$$
I(x - x_0, y - y_0)
$$
$$
= I_0 \left[1 + z^2 + \frac{1}{2}\beta_4(z^2)^2 + \frac{1}{6}\beta_6(z^2)^3 \right]^{-1} + I_s, \quad (5)
$$

with

$$
z^2 = \frac{1}{2}\left[\frac{(x - x_0)^2}{\sigma_x^2} + 2\sigma_{xy}(x - x_0)(y - y_0) + \frac{(y - y_0)^2}{\sigma_y^2}\right]. \quad (6)
$$

Following the recommended usage, we fix $\beta_4 = \beta_6 = 1$, such that the model is a truncated Gaussian power series. The free parameters are the shape parameters (σ_x, σ_{xy}, and σ_y), determined globally for an image, with the position (x_0, y_0) and the peak and sky intensities (I_0, I_s) determined for each object. DoPHOT is optimized for point-source photometry. The reported PSF flux is the integral under this analytic function, scaled by the measured peak intensity for each object. Photometry of ESSENCE galaxies will be addressed in future work and is not described here.

This instrumental photometry is then calibrated against a catalog of objects with known magnitudes, to determine the photometric zero point for the image. Further discussion of photometric calibrations follows in § 3.

2.2.5. Image Subtraction

Each image is then differenced against a reference image. This suppresses all constant sources of flux and reveals transients such as new supernovae. To subtract two images taken under different atmospheric conditions on different nights, we must correct for seeing variations. Our image subtraction software uses the algorithm devised by Alard and Lupton (Alard & Lupton 1998; Alard 2000) to determine and apply a convolution that matches the PSFs of the two images prior to subtraction. Improvements to the basic method have produced a process that automatically, robustly, and reliably produces clean subtractions in our data.

2.2.6. Difference Image Object Detection

Object detection in the subtracted (difference) images is done with a modified version of DoPHOT. Resampling and convolution of the images correlates flux between pixels, so we have modified the image registration and subtraction software to propagate noise maps that track these correlations. The variance is propagated through both stages, although the off-diagonal covariances introduced by remapping are not propagated through the image registration. Consequently, the raw noise maps slightly underestimate the true error, as described in § 4.4. These are then used to evaluate the significance of objects detected in the difference image.

2.3. Candidate Selection

Each observation of a single ESSENCE field yields hundreds of objects detected at a significance threshold of $S/N \geq 5$ in the subtracted images. These must be culled to produce a small set of objects that are very likely to be SNe Ia and merit spectroscopic observations with large telescopes. We first apply a series of software cuts, which include the following:

1. Require that the object has the same PSF (either the PSF measured by DoPHOT in the original image, or in the convolved template subtraction template, depending on which image was convolved for subtraction).
2. Veto detections with significant amounts of pixels having negative flux (30% within an aperture of radius $1.5 \times$ FWHM around the detection), to guard against subtraction residuals, such as dipoles resulting from slight image misalignment.
3. Veto variable sources identified in previous ESSENCE data (variable stars, active galactic nuclei [AGNs]).
4. Require coincident detections in more than one passband or on subsequent nights, to reject asteroids (two detections at $S/N > 5$ within a 5 day window).

While the above rules eliminate most of the false positives, we ultimately rely on human inspection to reject the small fraction of contaminants that evade these filters. Common problems include insufficient masking of pixels from bright stars, subtraction artifacts, and variable objects that have not varied significantly in previous ESSENCE data. Also, while the cuts above are used for the majority of the ESSENCE search, on a few occasions we have relaxed some of them (such as the requirement of two detections) when more candidates have been required for imminent spectroscopic observations.

We also perform light-curve fits to assess whether each object is consistent with the known behavior of SNe Ia. Preliminary fits of the initial R and I photometry are compared with light-curve templates of an SN Ia at $z = 0$ in B and V filters (which are a good match for SNe Ia at $z \approx 0.4$–0.5). The template light curve is representative of a normal SN Ia with $\Delta m_{15} = 1.1$ mag (Phillips 1993), or stretch $= 1$ (Goldhaber et al. 2001), and was constructed from well-sampled light curves of low-redshift SNe Ia (Prieto et al. 2006). Using a χ^2 minimization, we determine the best-fit values for time of B-band maximum, observed R and I magnitudes at maximum, and stretch. We chose to use stretch here because it parameterizes in a simple way the variety of light-curve shapes of SNe Ia (Goldhaber et al. 2001). Using the R and I magnitudes at maximum and the stretch obtained from the fit, we can now estimate a photometric redshift assuming that the candidate is an SN Ia. A standard ΛCDM model with $\Omega_M = 0.3$, $\Omega_\Lambda = 0.7$ is used, and no host galaxy reddening is considered in these fits.

A summary of the data for each candidate object is presented on a Web page for human inspection. We reject detections resulting from subtraction artifacts by looking at image "stamps" at the position of the supernova candidate. The light curves from the preliminary photometry enable us to reject objects that clearly have the wrong light-curve shape, color, and brightness for a supernova in the estimated redshift range.

Because our resources for spectroscopic follow-up observations are limited, we must make choices to observe the most promising targets. We select against objects right at the centers of galaxies, both because past experience has shown that these are frequently AGNs and because contamination from the galaxy often makes it impossible to positively identify the supernova in a spectrum. To avoid these problems, we select against candidates that are superposed on pointlike sources in the central pixel ($0.27''$) of the

template image. We know that the SNe Ia in galactic centers have a broader distribution in apparent luminosity than SNe Ia generally (Jha et al. 2007), but we do not expect any significant cosmological bias from this selection criterion.

The objects that pass the above selection procedure are then sent to team members for spectroscopic observations. Because time for spectroscopy is limited and scheduled in advance, we are forced to prioritize those objects that look most promising based on the data available at the time. Our survey is limited by spectroscopy: at the end of each observing campaign, many objects remain that have light curves resembling those of SNe Ia, but for which we were unable to obtain follow-up spectroscopy. Nevertheless, we successfully detect and confirm new SNe Ia at a rate of roughly one new object per night of 4 m Blanco observing.

3. SPECTROSCOPY

3.1. *Observations*

Follow-up spectroscopic observations of ESSENCE targets are performed at a wide variety of ground-based telescopes: the 10 m Keck I (+LRIS; Oke et al. 1995) and Keck II (+ESI, Sheinis et al. 2002; +DEIMOS, Faber et al. 2003) telescopes; the 8 m VLT (+FORS1; Appenzeller et al. 1998), Gemini North and South (+GMOS; Hook et al. 2003) telescopes; the 6.5 m Magellan Baade (+IMACS; Dressler 2004[22]) and Clay (+LDSS2; Mulchaey 2001[23]) telescopes; and the 6.5 m MMT (+BlueChannel; Schmidt et al. 1989). One target (d100.waa7_16; see Matheson et al. 2005) was confirmed as an SN Ia using the FAST spectrograph (Fabricant et al. 1998) on the 1.5 m Tillinghast Telescope at the F. L. Whipple Observatory (FLWO). The useful sample of objects from the ESSENCE program is limited by our ability to identify SNe Ia spectroscopically. The first two years of spectroscopy were published by Matheson et al. (2005) and are publicly available.[24] For more information concerning supernova candidate selection for spectroscopy, as well as the various telescope/instrument configurations used, we refer the reader to that paper.

Standard CCD processing and spectrum extraction are done with IRAF routines. Except for the VLT data, all the spectra are extracted using the optimal algorithm of Horne (1986). For the VLT data, we apply a novel extraction method based on two-channel Richardson-Lucy restoration (Blondin et al. 2005) to minimize contamination of the supernova spectrum by underlying galaxy light. The spectra are wavelength calibrated using calibration lamp spectra (usually HeNeAr). For the flux calibration we use both standard IRAF routines and our own IDL procedures, which include the removal of telluric lines using the well-exposed continua of the spectrophotometric standard stars (Wade & Horne 1988; Matheson et al. 2000a).

3.2. *Supernova Classification and Redshift Determination*

Supernovae are classified according to their early-time spectra (for a review see Filippenko 1997). The distinctive spectroscopic signature of an SN Ia near maximum light is a deep absorption feature due to Si II $\lambda6355$, blueshifted by $\sim$10,000 km s^{-1}. The spectra of SNe Ia are further characterized by the absence of hydrogen and helium lines, although hydrogen has been detected in the spectrum of the peculiar SN Ia SN 2002ic (Hamuy et al. 2003; Wood-Vasey et al. 2004) (but note that Benetti et al. [2006] classify this object as an SN Ib/c). Spectra of SNe Ib are

characterized by a weaker Si II $\lambda6355$ absorption and by the presence of lines of He I. Spectra of SNe Ic are devoid of He I lines and display only weak Si II $\lambda6355$ absorption. Thus, in principle, SNe Ib/c are readily distinguishable from SNe Ia.

At high redshifts ($z \gtrsim 0.4$), however, the defining Si II $\lambda6355$ feature in SNe Ia is redshifted out of the optical range of most of the spectrographs we use, so features blueward of this must be used to establish the type. The most prominent of these, the Ca II H and K $\lambda\lambda3934$, 3968 doublet, is also present in SNe Ib/c and does not discriminate between the various supernova types. Instead, the identification of SNe Ia relies on weaker features (e.g., Si II $\lambda4130$, Mg II $\lambda4481$, Fe II $\lambda4555$, Si III $\lambda4560$, S II $\lambda4816$, and Si II $\lambda5051$).

While the above gives the general defining features of SN Ia spectra, in practice the identification of SNe Ia can be difficult with low-S/N spectra, particularly when trying to discriminate between SNe Ia and SNe Ib/c. In addition, we would like to establish objective and reproducible criteria for classifying objects, rather than relying on subjective assessments of noisy data. Therefore, we have developed an algorithm (Supernova Identification, or SNID; Blondin & Tonry 2007) also used by Matheson et al. (2005), which we use here to establish our final SN Ia sample. This algorithm cross-correlates an input spectrum with a library of supernova spectra, without attempting to directly identify specific features, and a redshift is determined based on the shift in wavelength that maximizes the correlation. The spectral database currently spans all supernova types and covers a wide range of ages, containing 796 spectra of 64 SNe Ia (including spectra of SN 1991T–like and SN 1991bg–like objects), 288 spectra of 17 SNe Ib/c, and 353 spectra of 10 SNe II. We also include spectra of galaxies, AGNs, and stars to identify spectra that are not consistent with a supernova (see also Matheson et al. 2005). The results of the SNID analysis are shown in Table 3.

The SNID routine is based on the cross-correlation techniques of Tonry & Davis (1979). The input and template spectra are binned on a common logarithmic wavelength scale, such that a redshift corresponds to a uniform shift in ln λ. A pseudocontinuum is removed through division by a spline fit, which ensures that the correlation is insensitive to reddening, spectral colors, and flux calibration errors, and that only the relative shape of the spectral features is considered. The input spectrum is then cross-correlated with each template spectrum, and a correlation redshift, z_{cor}, is computed based on the highest peak in the resulting correlation function. We also compute a correlation parameter, r, as the ratio of the height of the correlation peak to the rms of the antisymmetric component of the correlation function about the correlation redshift (for a more detailed explanation see Matheson et al. 2005; Blondin & Tonry 2007). This correlation parameter is further weighted by the overlap in ln λ ("lap"), between the input and template spectrum at the correlation redshift, to ensure that sufficient spectral information is used in the correlation. As in Matheson et al. (2005), we only consider cross-correlations with $r(\mathrm{lap}) = r \times \mathrm{lap} \geq 5$ and $\mathrm{lap} = \ln(\lambda_1/\lambda_0) > 0.40$, where $[\lambda_0, \lambda_1]$ is the wavelength range of overlap between input and template spectra, at the correlation redshift. We show examples of correlation functions for three of our objects in Figure 4.

Once all of the template spectra have been cross-correlated with the input spectrum, an initial redshift is calculated as the $r(\mathrm{lap})$-weighted median of all correlation redshifts. The cross-correlation process is then repeated, this time masking out portions of the template and supernova spectra that do not overlap at this redshift. A new $r(\mathrm{lap})$-weighted median redshift, z_{wmed}, is computed, and cross-correlations that do not satisfy $r(\mathrm{lap}) > 5$, lap > 0.40, and $|z_{cor} - z_{\mathrm{wmed}}| < 0.02$ are discarded. The final redshift (z_{SNID}) is reported as the (nonweighted) median of all "good" correlation

---

[22] See http://www.lco.cl/telescopes-information/magellan/instruments-1/imacs-1/user-manual-1/user-manual.

[23] See http://www.lco.cl/telescopes-information/magellan/instruments-1/ldss-3-1/.

[24] See http://www.noao.edu/noao/staff/matheson/spectra.html.

TABLE 3
TYPES AND REDSHIFTS OF ESSENCE SUPERNOVAE

IAUC ID (1)	R.A. (J2000.0) (2)	Decl. (J2000.0) (3)	ESSENCE ID (4)	Type (5)	Subtype (6)	% Subtype (7)	% Ia (8)	% Ib/c (9)	% II (10)	$z_{\rm GAL}$ (11)	$z_{\rm SNID}$ (12)	σ_z (13)
2002iu	00 13 33.10	−10 13 09.92	b003	Ia	Ia-norm	74.2	100.0	0.0	0.0	...	0.115	0.006
2002iv	02 19 16.11	−07 44 06.72	b004	Ia	Ia-91T	64.4	98.3	1.7	0.0	0.231	0.226	0.003
2002jq	23 35 57.96	−10 05 56.88	b008	Ia	Ia-norm	65.1	81.4	11.6	7.0	...	0.474	0.004
2002iy	02 30 40.00	−08 11 40.50	b010	Ia	Ia-norm	73.6	82.4	17.6	0.0	0.587	0.590	0.006
2002iz	02 31 20.73	−08 36 13.12	b013	Ia	Ia-norm	85.8	98.6	1.4	0.0	0.428	0.426	0.004
2002ja	23 30 09.66	−09 35 01.75	b016	Ia	Ia-norm	100.0	100.0	0.0	0.0	...	0.329	0.003
2002jb	23 29 44.14	−09 36 34.25	b017	Ia	Ia-norm	75.5	100.0	0.0	0.0	...	0.258	0.007
2002jr	02 04 41.03	−05 09 40.73	b020	Ia	Ia-norm	81.8	100.0	0.0	0.0	...	0.425	0.003
2002jc	02 07 27.28	−03 50 20.73	b022	Ia	Ia-norm	55.7	65.7	24.3	10.0	...	0.540	0.008
2002js	02 20 35.39	−09 34 43.90	b023	Ia	Ia-norm	90.9	100.0	0.0	0.0	...	0.550	0.007
2002jd	00 28 38.39	+00 40 29.29	b027	Ia	Ia-norm	79.2	96.6	3.4	0.0	...	0.318	0.005
2002jt	00 13 36.70	−10 08 24.00	c003	Ia	[a]	...	100.0	0.0	0.0	...	0.382	0.002
2002ju	02 20 11.00	−09 04 37.50	c012	Ia	Ia-norm	72.6	100.0	0.0	0.0	0.348	0.350	0.006
2002jw	02 30 00.52	−08 36 22.41	c015	Ia	Ia-norm	76.6	100.0	0.0	0.0	0.357	0.362	0.008
2002jw	00 28 03.16	+00 37 50.43	c023	Ia	Ia-norm	100.0	100.0	0.0	0.0	0.399	0.400	0.009
2003jo	23 25 24.03	−09 26 00.63	d033	Ia	Ia-norm	76.0	96.0	4.0	0.0	0.524	0.531	0.008
2003jj	01 07 58.52	+00 03 01.89	d058	Ia	Ia-norm	85.0	95.0	5.0	0.0	0.583	0.583	0.009
2003jn	02 29 21.21	−09 02 15.57	d083	Ia	Ia-91T	56.5	100.0	0.0	0.0	...	0.333	0.002
2003jm	02 28 50.93	−09 09 58.14	d084	Ia	Ia-norm	68.6	100.0	0.0	0.0	0.522	0.519	0.007
2003jv	23 27 58.22	−08 57 11.82	d085	Ia	Ia-91T	100.0	100.0	0.0	0.0	0.405	0.401	0.001
2003ju	23 27 01.71	−09 24 04.49	d086	Ia	Ia-norm	87.5	100.0	0.0	0.0	...	0.205	0.003
2003jr	01 11 06.23	+00 13 44.21	d087	Ia	Ia-norm	100.0	100.0	0.0	0.0	0.340	0.337[b]	0.009
2003jl	02 28 28.56	−08 08 44.74	d089	Ia	Ia-norm	92.3	100.0	0.0	0.0	0.429	0.436	0.006
2003js	02 29 52.15	−08 32 28.09	d093	Ia	Ia-91T	63.1	93.4	6.6	0.0	0.363	0.360	0.004
2003jt	02 31 54.60	−08 35 48.43	d097	Ia	Ia-norm	95.7	100.0	0.0	0.0	...	0.436	0.008
2003ji	02 07 54.84	−03 28 28.40	d099	Ia	Ia-norm	77.5	96.9	2.0	1.0	...	0.211	0.003
2003jq	23 30 51.19	−09 28 33.95	d100	Ia	Ia-norm	67.8	98.3	1.7	0.0	...	0.156	0.003
2003jw	02 31 06.84	−08 45 36.51	d117	Ia	Ia-norm	84.6	100.0	0.0	0.0	0.296	0.309	0.006
2003jy	02 10 53.98	−04 25 49.76	d149	Ia	Ia-norm	100.0	100.0	0.0	0.0	0.339	0.342	0.006
2003kk	23 25 36.06	−09 31 44.70	e020	Ia	Ia-norm	88.4	100.0	0.0	0.0	0.164	0.159	0.007
2003kl	01 09 48.80	+01 00 05.58	e029	Ia	Ia-norm	74.7	100.0	0.0	0.0	0.335	0.332	0.008
2003km	02 30 01.00	−09 04 35.89	e108	Ia	Ia-norm	100.0	100.0	0.0	0.0	...	0.469	0.005
2003kn	02 09 15.55	−03 35 41.38	e132	Ia	Ia-norm	76.3	100.0	0.0	0.0	0.244	0.239	0.006
2003ko	02 11 06.48	−03 47 56.09	e136	Ia	Ia-norm	85.1	99.2	0.8	0.0	0.360	0.352	0.007
2003kt	02 33 47.01	−08 36 22.09	e138	Ia	Ia-norm	100.0	100.0	0.0	0.0	...	0.612	0.009
2003kq	02 31 04.09	−08 10 56.64	e140	Ia	Ia-norm	100.0	100.0	0.0	0.0	0.606	0.631	0.007
2003kp	02 31 02.64	−08 39 50.81	e147	Ia	Ia-norm	100.0	100.0	0.0	0.0	...	0.645	0.010
2003kr	02 31 20.96	−08 36 14.16	e148	Ia	Ia-norm	100.0	100.0	0.0	0.0	0.427	0.429	0.006
2003ks	02 31 34.54	−08 36 46.41	e149	Ia	Ia-norm	81.4	98.6	1.4	0.0	...	0.497	0.006
2003ku[c]	01 08 36.25	−00 33 20.78	e315	...	...	...	...	...	...	...	...	...
2003kv[c]	02 09 42.52	−03 46 48.58	e531	...	...	...	...	...	...	...	...	...
2003lh	02 10 19.51	−04 59 32.30	f011	Ia	Ia-norm	100.0	100.0	0.0	0.0	...	0.539	0.004
2003le	01 08 08.73	+00 27 09.74	f041	Ia	Ia-norm	68.8	100.0	0.0	0.0	...	0.561	0.006
2003lf	01 08 49.81	−00 44 13.49	f076	Ia	Ia-norm	82.2	100.0	0.0	0.0	...	0.410	0.007
2003lm	23 24 25.51	−08 45 51.11	f096	Ia	Ia-norm	88.5	100.0	0.0	0.0	0.408	0.412	0.006
2003ll	02 35 41.19	−08 06 29.55	f216	Ia	Ia-norm	75.0	100.0	0.0	0.0	0.596	0.599	0.005
2003lk[d]	02 11 12.82	−04 13 52.11	f221	...	...	...	33.3	66.7	0.0	0.442	...	...
2003ln	23 30 27.15	−08 35 46.98	f231	Ia	Ia-norm	100.0	100.0	0.0	0.0	...	0.619	0.008
2003lj	01 12 10.03	+00 19 51.29	f235	Ia	Ia-norm	87.8	100.0	0.0	0.0	0.417	0.422	0.007
2003li	02 27 47.29	−07 33 46.16	f244	Ia	Ia-norm	100.0	100.0	0.0	0.0	0.544	0.540	0.004
2003li[d]	02 27 26.51	−08 42 24.88	f301	...	...	50.0	75.0	14.3	10.7	...	...	...
2003li	02 29 22.39	−08 37 38.38	f308	Ia	Ia-norm	66.7	100.0	0.0	0.0	...	0.394	0.009
2004fi[c]	23 29 45.35	−08 54 36.34	g001	...	...	...	...	...	...	0.265	...	...
2004fh	23 28 27.20	−08 36 55.17	g005	Ia	Ia-norm	72.9	100.0	0.0	0.0	...	0.218	0.007
2004fj	01 09 51.07	+00 27 20.95	g043	II	IIP	100.0	0.0	0.0	100.0	0.187	0.193	0.002
2004fn	23 30 20.12	−09 58 30.67	g050	Ia	Ia-norm	100.0	100.0	0.0	0.0	0.605	0.633	0.006
2004fm	23 26 58.14	−09 37 19.45	g052	Ia	Ia-norm	80.0	100.0	0.0	0.0	...	0.383	0.008
2004fl[c]	23 26 57.92	−09 37 19.11	g053	...	...	...	...	...	...	...	...	...
2004fk	01 13 35.84	−00 09 27.56	g055	Ia	Ia-norm	79.3	100.0	0.0	0.0	0.296	0.302	0.006
2004fk	23 27 37.16	−09 35 20.96	g097	Ia	Ia-norm	62.8	81.4	18.6	0.0	0.343	0.340	0.004
2004fo	01 13 28.97	+00 35 16.26	g120	Ia	Ia-norm	94.7	100.0	0.0	0.0	...	0.510	0.009
2004fo	02 09 49.63	−04 10 55.07	g133	Ia	Ia-norm	75.0	98.8	0.0	1.2	...	0.421	0.003
2004fo	23 28 37.70	−08 45 04.01	g142	Ia	Ia-norm	58.2	98.5	1.5	0.0	0.404	0.399	0.003
2004fq[c]	23 27 45.64	−08 31 12.77	g151	...	...	...	...	...	...	0.146	...	...

TABLE 3—*Continued*

IAUC ID (1)	R.A. (J2000.0) (2)	Decl. (J2000.0) (3)	ESSENCE ID (4)	Type (5)	Subtype (6)	% Subtype (7)	% Ia (8)	% Ib/c (9)	% II (10)	$z_{\rm GAL}$ (11)	$z_{\rm SNID}$ (12)	σ_z (13)
2004fs................	02 31 19.95	−08 49 21.67	g160	Ia	Ia-norm	89.5	100.0	0.0	0.0	. . .	0.493	0.003
2004fr[c]............	02 28 43.77	−08 54 24.05	g166	. . .	. . .	. . .	. . .	. . .	. . .	0.202	. . .	. . .
2004ft[c]............	02 33 32.63	−08 09 34.10	g199	. . .	. . .	. . .	. . .	. . .	. . .	. . .	. . .	. . .
2004ft[c]............	23 27 15.69	−09 27 59.76	g225	. . .	. . .	. . .	. . .	. . .	. . .	. . .	. . .	. . .
2004ft[d]............	01 11 56.31	+00 07 27.71	g230	. . .	. . .	. . .	50.0	0.0	50.0	0.392	. . .	. . .
2004ft................	23 30 41.83	−08 34 10.98	g240	Ia	Ia-norm	86.7	100.0	0.0	0.0	. . .	0.687	0.005
2004ft[c]............	02 04 27.01	−03 35 43.72	g276	. . .	. . .	. . .	. . .	. . .	. . .	0.244	. . .	. . .
2004ha................	02 04 27.01	−04 52 46.03	h283	Ia	Ia-norm	85.7	100.0	0.0	0.0	. . .	0.502	0.008
2004ha................	02 31 40.67	−08 49 03.35	h300	Ia	Ia-norm	100.0	100.0	0.0	0.0	. . .	0.687	0.012
2004hc................	23 24 32.67	−08 41 03.55	h311	Ia	Ia-norm	100.0	100.0	0.0	0.0	. . .	0.741[b]	0.011
2004hd................	02 08 48.21	−04 26 10.42	h319	Ia	Ia-norm	100.0	100.0	0.0	0.0	0.490	0.495	0.004
2004he................	02 29 48.79	−08 20 45.94	h323	Ia	Ia-norm	100.0	100.0	0.0	0.0	0.598	0.603	0.006
2004hf................	02 32 00.14	−08 42 23.89	h342	Ia	Ia-norm	100.0	100.0	0.0	0.0	. . .	0.421	0.002
2004hg[c]............	02 34 55.19	−08 30 43.64	h345	. . .	. . .	. . .	. . .	. . .	. . .	. . .	. . .	. . .
2004hi	02 08 38.84	−05 08 11.79	h359	Ia	Ia-norm	46.8	68.1	31.9	0.0	. . .	0.348	0.004
2004hh................	02 06 25.02	−04 38 04.09	h363	Ia	Ia-norm	69.0	97.7	0.0	2.3	. . .	0.213	0.006
2004hj	02 29 41.94	−08 43 49.42	h364	Ia	Ia-norm	100.0	100.0	0.0	0.0	. . .	0.344	0.007
2004hk[c]............	23 27 04.39	−08 38 45.11	k396	. . .	. . .	. . .	. . .	. . .	. . .	. . .	. . .	. . .
2004hk................	23 26 11.77	−08 50 17.50	k411	Ia	Ia-norm	78.6	85.7	14.3	0.0	. . .	0.564	0.006
2004hl	01 13 38.17	−00 27 39.03	k425	Ia	Ia-norm	82.9	97.1	0.0	2.9	0.270	0.274	0.003
2004hm	02 28 03.12	−07 42 29.70	k429	Ia	Ia-norm	66.7	100.0	0.0	0.0	0.172	0.181	0.008
2004hn................	01 13 32.39	+00 37 15.38	k430	Ia	Ia-norm	100.0	100.0	0.0	0.0	. . .	0.582	0.010
2004hn[c]............	01 13 38.17	−00 27 39.03	k432	. . .	. . .	. . .	. . .	. . .	. . .	. . .	. . .	. . .
2004hq................	02 30 18.04	−08 22 25.01	k441	Ia	Ia-norm	81.0	100.0	0.0	0.0	. . .	0.680	0.010
2004hp[c]............	02 09 35.52	−03 46 23.53	k443	. . .	. . .	. . .	. . .	. . .	. . .	. . .	. . .	. . .
2004hr	01 08 48.34	+00 00 49.49	k448	Ia	Ia-norm	100.0	100.0	0.0	0.0	0.409	0.401	0.005
2004hr[c]............	02 31 11.80	−07 47 34.13	k467	. . .	. . .	. . .	. . .	. . .	. . .	. . .	. . .	. . .
2004hs................	02 09 33.69	−04 13 03.93	k485	Ia	Ia-norm	93.3	100.0	0.0	0.0	. . .	0.416	0.005
2004hs[c]............	02 30 24.32	−07 53 20.95	k490	. . .	. . .	. . .	. . .	. . .	. . .	0.715	. . .	. . .
2004hs[c]............	01 08 22.01	−00 05 46.65	m001	. . .	. . .	. . .	. . .	. . .	. . .	. . .	. . .	. . .
2004hs................	02 05 27.31	−04 42 54.05	m003	II	[a]	34.2	2.6	0.0	97.4	. . .	0.219	0.001
2004hs[c]............	02 30 27.27	−09 16 10.23	m006	. . .	. . .	. . .	. . .	. . .	. . .	0.057	. . .	. . .
2004hs................	02 31 46.24	−09 16 25.65	m010	Ib	Ib-norm	100.0	0.0	100.0	0.0	0.216	0.222	0.001
2004hs................	02 08 06.23	−04 03 51.16	m011	II	IIP	78.1	0.0	0.0	100.0	0.205	0.211	0.002
2004hs................	02 07 12.91	−04 26 40.06	m014	II	IIP	50.0	0.0	0.0	100.0	0.200	0.212	0.003
2004hs................	23 30 02.70	−08 33 36.57	m022	Ia	[a]	. . .	93.8	1.8	4.4	. . .	0.240	0.003
2004hs................	23 28 39.97	−09 19 50.00	m026	Ia	[a]	. . .	97.8	2.2	0.0	0.655	0.653	0.008
2004hs................	01 09 15.01	+00 08 14.80	m027	Ia	Ia-norm	72.2	92.6	7.4	0.0	0.289	0.286	0.006
2004hs................	23 29 35.34	−09 58 46.33	m032	Ia	Ia-norm	80.2	96.5	3.5	0.0	. . .	0.155	0.004
2004hs................	02 27 50.33	−07 59 11.62	m034	Ia	Ia-norm	96.3	100.0	0.0	0.0	0.557	0.562	0.006
2004hs................	02 05 10.83	−04 47 13.94	m038	II	IIP	94.4	5.6	0.0	94.4	0.051	0.054	0.003
2004hs................	02 28 04.63	−07 42 44.29	m039	Ia	Ia-norm	84.4	100.0	0.0	0.0	0.248	0.249	0.003
2004hs................	02 09 49.78	−04 45 10.65	m041	II	[a]	. . .	22.8	0.0	77.2	. . .	0.220	0.004
2004hs................	23 29 51.73	−08 56 46.07	m043	Ia	Ia-norm	57.3	99.5	0.0	0.5	0.266	0.266	0.003
2004hs................	02 10 56.77	−04 27 29.90	m057	Ia	[a]	. . .	95.5	0.4	4.1	0.180	0.184	0.003
2004hs................	01 09 52.90	+00 36 19.03	m062	Ia	[a]	. . .	100.0	0.0	0.0	0.314	0.317	0.005
2004hs................	23 24 42.28	−08 29 07.82	m075	Ia	[a]	. . .	100.0	0.0	0.0	0.100	0.102	0.001
2004hs................	01 08 56.35	+00 39 25.38	m138	Ia	Ia-norm	66.7	100.0	0.0	0.0	0.587	0.582	0.004
2004hs................	23 23 57.83	−08 27 08.33	m139	II	[a]	. . .	0.0	0.0	100.0	0.212	. . .	. . .
2004hs................	23 24 03.53	−09 23 18.24	m158	Ia	[a]	. . .	95.2	4.8	0.0	. . .	0.463	0.007
2004hs................	02 28 52.20	−07 42 09.78	m193	Ia	Ia-norm	100.0	100.0	0.0	0.0	0.330	0.341	0.009
2004hs................	02 06 03.69	−04 39 59.12	m226	Ia	[a]	. . .	95.2	4.8	0.0	0.675	0.671	0.004
2004hs[c]............	01 14 33.08	−00 26 23.18	n246	. . .	. . .	. . .	. . .	. . .	. . .	0.706	. . .	. . .
2004hs................	02 28 09.01	−07 47 49.56	n256	Ia	Ia-norm	100.0	100.0	0.0	0.0	. . .	0.631	0.012
2004hs................	02 06 42.35	−04 22 37.01	n258	Ia	Ia-norm	50.0	81.6	18.4	0.0	. . .	0.522	0.007
2004hs................	02 05 14.95	−04 56 39.08	n263	Ia	Ia-norm	79.9	100.0	0.0	0.0	. . .	0.368	0.007
2004hs................	01 13 06.51	+00 30 04.86	n271	II	IIP	85.2	0.0	0.0	100.0	. . .	0.241	0.004
2004hs................	23 28 17.55	−09 23 12.38	n278	Ia	Ia-norm	78.5	100.0	0.0	0.0	0.304	0.309	0.006
2004hs................	23 23 51.35	−08 23 18.47	n285	Ia	Ia-norm	64.5	81.4	14.5	4.1	. . .	0.528	0.006
2004hs[c]............	02 29 00.48	−09 02 52.96	n322	. . .	. . .	. . .	. . .	. . .	. . .	. . .	. . .	. . .
2004hs................	23 29 58.59	−08 53 12.45	n326	Ia	Ia-norm	79.8	100.0	0.0	0.0	0.264	0.268	0.006
2004hs................	23 30 32.01	−10 03 22.14	n368	Ia	Ia-norm	83.1	100.0	0.0	0.0	0.342	0.344	0.006
2004hs[c]............	01 13 13.26	−00 23 25.86	n400	. . .	. . .	. . .	. . .	. . .	. . .	0.424	. . .	. . .
2004hs................	02 31 31.43	−08 55 11.52	n404	Ia	Ia-norm	100.0	100.0	0.0	0.0	. . .	0.216	0.008
2004hs[c]............	02 31 19.60	−08 45 09.76	n406	. . .	. . .	. . .	. . .	. . .	. . .	. . .	. . .	. . .

TABLE 3—*Continued*

IAUC ID (1)	R.A. (J2000.0) (2)	Decl. (J2000.0) (3)	ESSENCE ID (4)	Type (5)	Subtype (6)	% Subtype (7)	% Ia (8)	% Ib/c (9)	% II (10)	z_{GAL} (11)	z_{SNID} (12)	σ_z (13)
2004hs..............	23 29 56.19	−08 34 24.34	p425	Ia	Ia-norm	100.0	100.0	0.0	0.0	0.458	0.453	0.006
2004hs[c]............	01 12 40.25	+00 14 56.61	p434	...	...	...	61.7	33.3	4.9	0.339	...	...
2004hs..............	02 08 32.45	−03 33 34.20	p454	Ia	Ia-norm	100.0	100.0	0.0	0.0	...	0.695	0.010
2004hs..............	02 11 00.02	−04 09 37.59	p455	Ia	Ia-norm	88.9	100.0	0.0	0.0	0.298	0.284	0.006
2004hs[c]............	02 08 09.34	−03 48 05.05	p520	...	...	...	...	...	...	...	...	...
2004hs..............	02 30 10.16	−08 52 50.84	p524	Ia	Ia-norm	100.0	100.0	0.0	0.0	...	0.508[b]	0.009
2004hs[c]............	02 08 10.47	−03 32 17.70	p527	...	...	...	...	...	...	0.435	...	...
2004hs..............	02 07 04.66	−03 28 04.37	p528	Ia	Ia-norm	88.2	100.0	0.0	0.0	0.781	0.777	0.005
2004hs..............	02 04 56.09	−03 49 03.67	p534	Ia	Ia-norm	79.1	100.0	0.0	0.0	0.619	0.615	0.008

NOTES.—Units of right ascension are hours, minutes, and seconds, and units of declination are degrees, arcminutes, and arcseconds. Col. (1): Official IAU supernova designation; note that not all objects listed here have official International Astronomical Union names. Col. (2): Right ascension. Col. (3): Declination. Col. (4): ESSENCE internal identification. Col. (5): Supernova type as determined using SNID (see text for details). Col. (6): Supernova subtype as determined using SNID (see text for details). Col. (7): Absolute fraction of supernova templates corresponding to the supernova subtype listed in col. (6). Col. (8): Absolute fraction of supernova templates corresponding to SNe Ia. Col. (9): Absolute fraction of supernova templates corresponding to SNe Ib or SNe Ic. Col. (10): Absolute fraction of supernova templates corresponding to SNe II. Col. (11): Redshift measured from narrow emission or absorption lines from the host galaxy. Col. (12): Redshift as determined using SNID (see text for details). Col. (13): Redshift error on the SNID redshift (see text for details).

[a] A secure type was determined, but not a secure subtype: there was a majority of correlations with one subtype, but the best match template was of a different subtype.

[b] Only one template that exceeds the cutoff for "good" correlations: the reported redshift is that of the best match template (as opposed to the median redshift), and the associated error is the formal redshift error for that template (see Blondin & Tonry 2007).

[c] No "good" correlations for this object. No type or redshift information is reported.

[d] While there were "good" correlations for this object, a secure type could not be determined, and we report no redshift for this object.
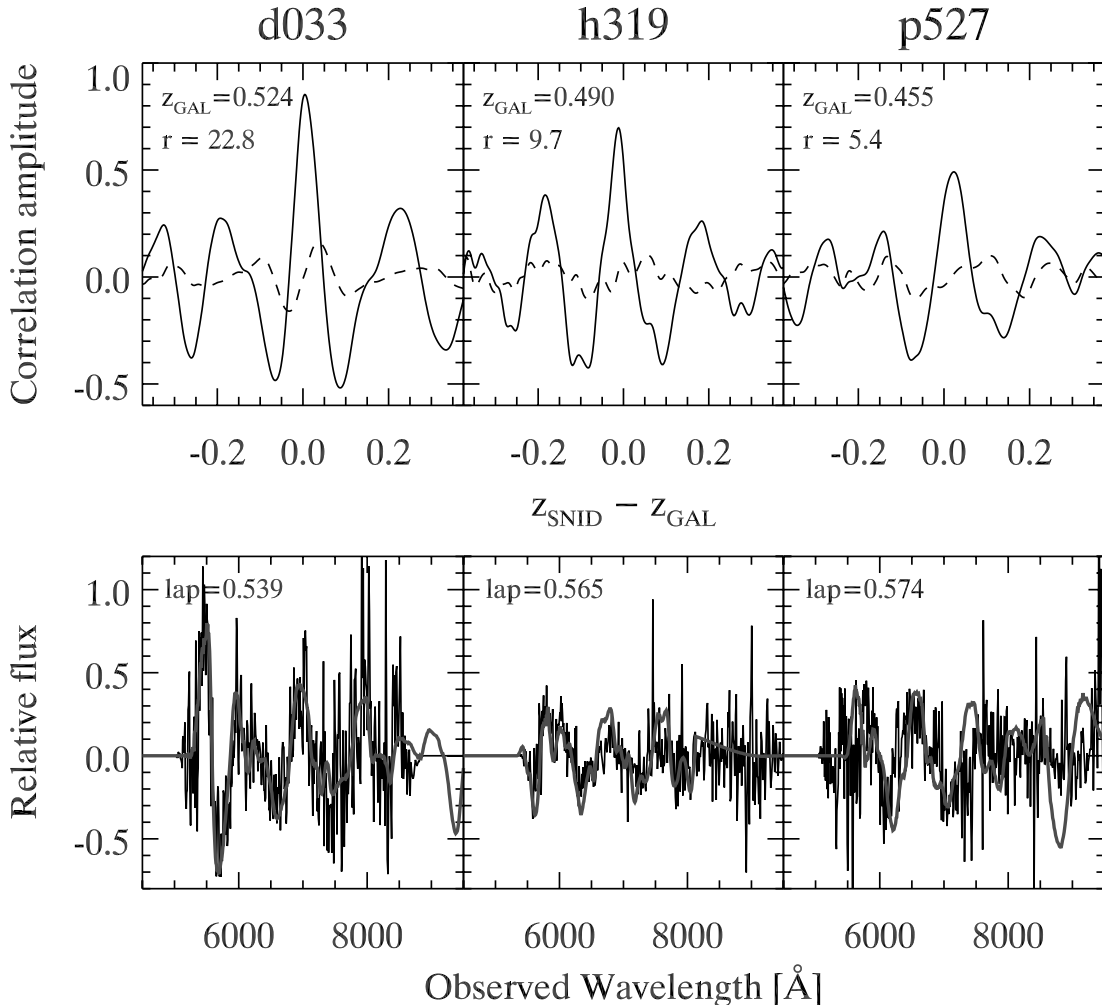
FIG. 4.—*Top*: Examples of normalized correlation functions (*solid line*), for three objects in our sample. The abscissa corresponds to the difference between the correlation redshift (z_{SNID}) and the galaxy redshift (z_{GAL}). The *r*-value is defined as the ratio of the height of the highest peak in the correlation function to the rms of its antisymmetric component (*dashed line*). The higher the *r*-value, the better the correlation. *Bottom*: Input spectrum (*black*) and best match template (*gray*) for each object. We also give the overlap in logarithmic wavelength space between the input and template spectrum at the correlation redshift (lap). "Good" correlations are those for which r(lap) $\geq$ 5 (for details see Blondin & Tonry 2007). While both d033 and h319 are classified as SNe Ia based on this technique, p527 is discarded from the sample due to its poor correlation with an SN Ia template. [*See the electronic edition of the Journal for a color version of this figure.*]

redshifts that satisfy the above condition (Matheson et al. 2005). The redshift error (σ_z) is simply reported as the standard deviation of the redshifts used to compute z_{SNID}.

The correlation redshift is valid when templates of the correct supernova type are used. We also use SNID to determine the supernova type, by computing the absolute fraction of "good" correlations that correspond to supernovae of different types. The supernova types/subtypes in the SNID spectral database are Ia/Ia-norm, Ia-pec, Ia-91T, Ia-91bg; Ib/Ib-norm, Ib-pec, IIb; Ic/Ic-norm, Ic-pec, Ic-broad; II/II-norm, II-pec, IIL, IIn, IIP, and IIb. "Norm" and "pec" subtypes are used to identify the spectroscopically "normal" and "peculiar" supernovae of a given type, respectively. For SNe Ia, "91T" and "91bg" indicate spectra that resemble those of the overluminous SN 1991T and the underluminous SN 1991bg, respectively. The spectra that correspond to the "Ia-pec" category in this case are those of SN 2000cx (Li et al. 2001b; Candia et al. 2003) and SN 2002cx (Li et al. 2003). For SNe Ic, "Ic-broad" is used to identify broad-lined SNe Ic (often referred to as "hypernovae" in the literature), some of which are associated with gamma-ray bursts. The notations adopted for the Type II subtypes are commonly used in the literature. Note that SNe IIb (whose spectra evolve from a Type II to a Type Ib, as, for example, in SN 1993J; see Filippenko et al. 1993; Matheson et al. 2000b) are included in both the "Ib" and "II" types.

If the redshift of the supernova host galaxy can be measured using narrow emission or absorption lines, we force SNID to look for correlations at the galaxy redshift (±0.03) to determine the supernova type/subtype; otherwise, the redshift is left as a free parameter. We assert a supernova to be of a given type (i.e., Ia, Ib, Ic, II; see Table 3, col. [3]) when the absolute fraction of "good" correlations that correspond to this type exceeds 50%. A "good" correlation is defined to have an associated $r(\text{lap}) \geq 5$, where r is the Tonry & Davis (1979) r-value and lap is the overlap in logarithmic wavelength space between the input and template spectra at the correlation redshift (Blondin & Tonry 2007; see also Matheson et al. 2005). We require that lap ≥ 0.4 to ensure sufficient wavelength overlap between the input and template spectra. Blondin & Tonry (2007) show that requiring 50% good correlations is sufficient to guard against contamination from SNe Ic, as well as distinguishing SN 1991T–like objects from other SNe Ia. In addition, we require the best match supernova template to be of the same type. We determine the supernova subtype by requiring that the absolute fraction of "good" correlations that correspond to this subtype exceeds 50%, *and* that it corresponds to the previously determined type. We also require that the best match supernova template is of the same subtype.

The requirement that an object must have a correlation fraction above 50% is motivated by the desire to have a quantitative figure of merit that determines when the spectral information is strong enough to make a positive identification. Out of all the spectra that were considered to be those of possible supernovae, 28 did not meet the above criterion for a positive classification (see Table 3). Assessing the likelihood that a spectrum matches that of a particular known object more closely than others is a challenging statistical problem, especially in the presence of intrinsic and only partially understood variance in the populations of supernovae. See Blondin & Tonry (2007) for a detailed discussion of ongoing work to better understand these issues.

The redshift is then determined from the supernova spectrum alone in a second SNID run by considering correlations with templates of the determined type and subtype. No a priori information on redshift is used in this second run. The supernova redshift is reported as the median redshift of all "good" correlations, and the redshift uncertainty as the standard deviation of these same red-
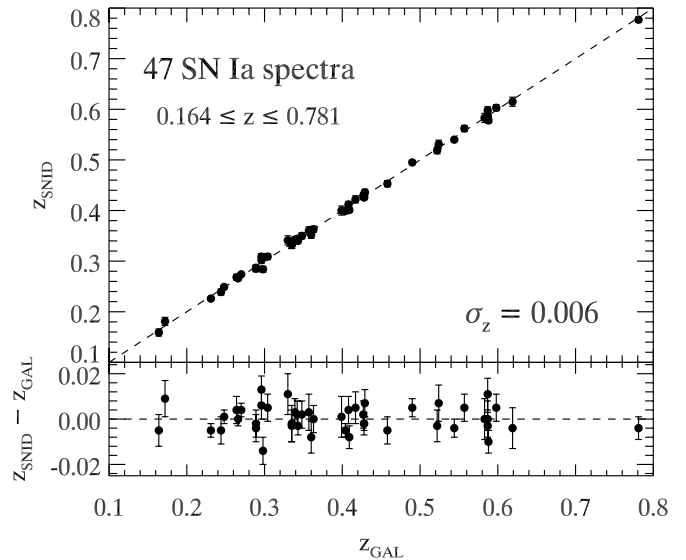
FIG. 5.—Comparison of ESSENCE SN Ia redshifts obtained from narrow emission and/or absorption lines in the host galaxy spectrum (z_{GAL}) and from cross-correlations with a library of SN Ia spectral templates (z_{SN}). The correspondence is excellent, with a standard deviation of only $\sim$0.006 (see also Matheson et al. 2005). The reduced χ^2 for the linear fit is 0.99, indicating that the redshift uncertainties are correct. Only the 47 ESSENCE supernovae for which it was possible to measure host galaxy redshifts are used.

shifts. Unlike the standard cross-correlation procedure for measuring galaxy redshifts, in which the best-fit template is selected, here the median redshift is chosen, since supernova spectra (unlike galaxy spectra) have a strong variance at a given phase and evolve with time. Furthermore, the distribution of redshift residuals is Gaussian in this case, whereas it is not (and even nonuniform) for the redshift associated with the best match template (Blondin & Tonry 2007). When there is only one "good" correlation for an input spectrum (objects d087, h311, and p524 in Table 3), we quote the redshift as that of the best match template and the associated uncertainty as the formal redshift error for that template (see Blondin & Tonry 2007).

We only report an SN redshift when a secure type is determined. In Matheson et al. (2005) we found an excellent agreement between the SNID correlation redshift and the redshift of the supernova host galaxy when it is known from other methods. Figure 5 again shows that the SNID redshifts agree well with the galaxy redshifts, with a typical uncertainty $\lesssim0.01$ in the redshift range 0.1–0.8. Figure 6 shows the redshift distribution of the spectroscopically confirmed SNe Ia from the first four years of ESSENCE.

4. PHOTOMETRY OF ESSENCE SUPERNOVAE

4.1. *Importance of Photometric Calibration*

Our ability to determine cosmological parameters from the observations of SNe Ia depends on measuring the fluxes of these objects accurately. Errors in photometric calibration translate into errors in the cosmology in two basic ways. First, we must understand the calibration of our supernova fluxes to those of the low-redshift sample (Hamuy et al. 1993; Riess et al. 1999a; Jha et al. 2006). Light-curve fitting and luminosity estimation methods have been trained using these objects, and they also serve the "anchor" for the Hubble diagram in our cosmological measurements of the evolution of the scale factor. Second, accurate passband-to-passband calibration is important for estimating the colors of our SNe Ia, to provide constraints on extinction due to host galaxy dust. See Wood-Vasey et al. (2007) for a
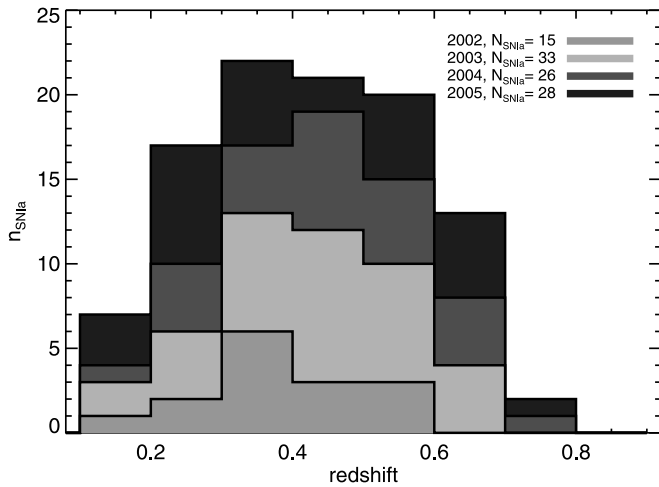
FIG. 6.—Redshift histogram of spectroscopically confirmed ESSENCE SNe Ia (all objects whose Type Ia correlations exceed 50%). [*See the electronic edition of the Journal for a color version of this figure.*]
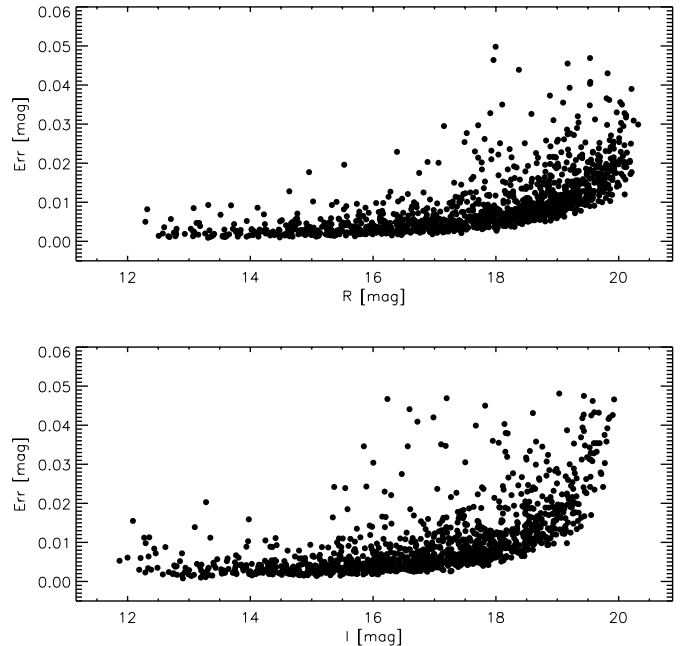

FIG. 7.—Uncertainty in 0.9 m photometry of ESSENCE field stars as a function of *R*-band magnitude (*top*) and *I*-band magnitude (*bottom*). Individual stars are typically measured to a precision of 2% or better.

discussion of how these calibration issues impact our cosmological measurements.

Photometric systems are defined by the broadband fluxes of a single standard star (conventionally Vega, although more recently SDSS and other surveys have used the F0 subdwarf BD +17 4708), as well as a network of standard stars whose fluxes have been calibrated relative to the primary standard (Landolt 1983, 1992) and the wavelength-dependent sensitivities of that system. Observers usually account for the difference between the particular system they are using and the standard system by correcting their observations through terms proportional to the broadband colors. These linear corrections can be quite accurate when derived from observations of standard stars and then applied to correct the photometry of other observed stars, since stellar spectra are generally relatively smooth. However, SNe Ia have complex spectra with broad and deep features, and they evolve with time, so the corrections derived from observations of stars are not appropriate for calibrating supernova fluxes into a standard system.

To avoid additional error from converting the observed supernova fluxes to a "standard" system, we report our photometry in the natural system of the CTIO 4 m MOSAIC camera:

$$m = -2.5 \log \mathcal{F}(\mathrm{ADU}) + \mathrm{zero\ point}, \tag{7}$$

where the zero points are defined relative to the star Vega. It is important to note that in the process of defining a Vega-based standard-star system, the "true" magnitudes of Vega have actually drifted and are slightly nonzero (Bessell et al. 1998; Bohlin & Gilliland 2004; Bohlin 2007). While these offsets amount to changes in the flux scale of only a few percent, they become significant for cosmological measurements at the level of precision we desire and must be accounted for (for our treatment of these in the cosmological analysis see Wood-Vasey et al. 2007).

In the following sections we describe the calibration of the ESSENCE photometry in the CTIO 4 m telescope natural system.

4.2. *Calibration of ESSENCE Field Stars*

To establish a Vega-based natural system in our ESSENCE fields, we tie the stars in these fields to the secondary standards of Landolt (1983, 1992). Unfortunately, the overhead in acquiring a sufficient number of observations of these stars with the MOSAIC imager

is quite high (∼100 s readout time, with additional time spent changing filters and pointing the telescope) relative to the very short exposures needed to observe these bright objects on a 4 m class telescope. Therefore, we have elected to calibrate stars in our fields with an auxiliary program using the CTIO 0.9 m telescope. Concurrent with the ESSENCE program, we have used 16 photometric nights on the 0.9 m telescope to observe both Landolt standards and ESSENCE field stars, resulting in 32 calibration patches within the ESSENCE survey. Each patch contains 40–60 stars observed on a minimum of three photometric nights. The quality of the photometric calibrations resulting from the 0.9 m program is quite good, with individual stars calibrated to ∼1%. Figure 7 shows the error in the mean magnitude of each star resulting from a simultaneous fit to all 0.9 m observations of these stars, weighted by their errors, which include contributions from uncertainties in the PSF, standard-star magnitudes, and the photometric solutions.

4.3. *CTIO* 4 m *Photometric Zero Points*

While the 0.9 m photometry allows for the transfer of photometric calibrations in the Vega system to our 4 m data, it is not sufficient to calibrate all of our ESSENCE data, due to the small (13′) field of view relative to the MOSAIC imager. Each 0.9 m patch allows us to calibrate data from only one of the eight CCDs in the CTIO MOSAIC. Therefore, by using our own data taken on photometric nights and carefully propagating photometric zero points from the overlapping data to the rest of the MOSAIC, we generate catalogs that cover our fields completely. These catalogs effectively define the ESSENCE photometric system and are used to calibrate data taken on all other nights.

First, we must transform the 0.9 m magnitudes from the system defined by the Landolt (1992) standard stars to the CTIO MOSAIC natural photometric system, via equations of the form

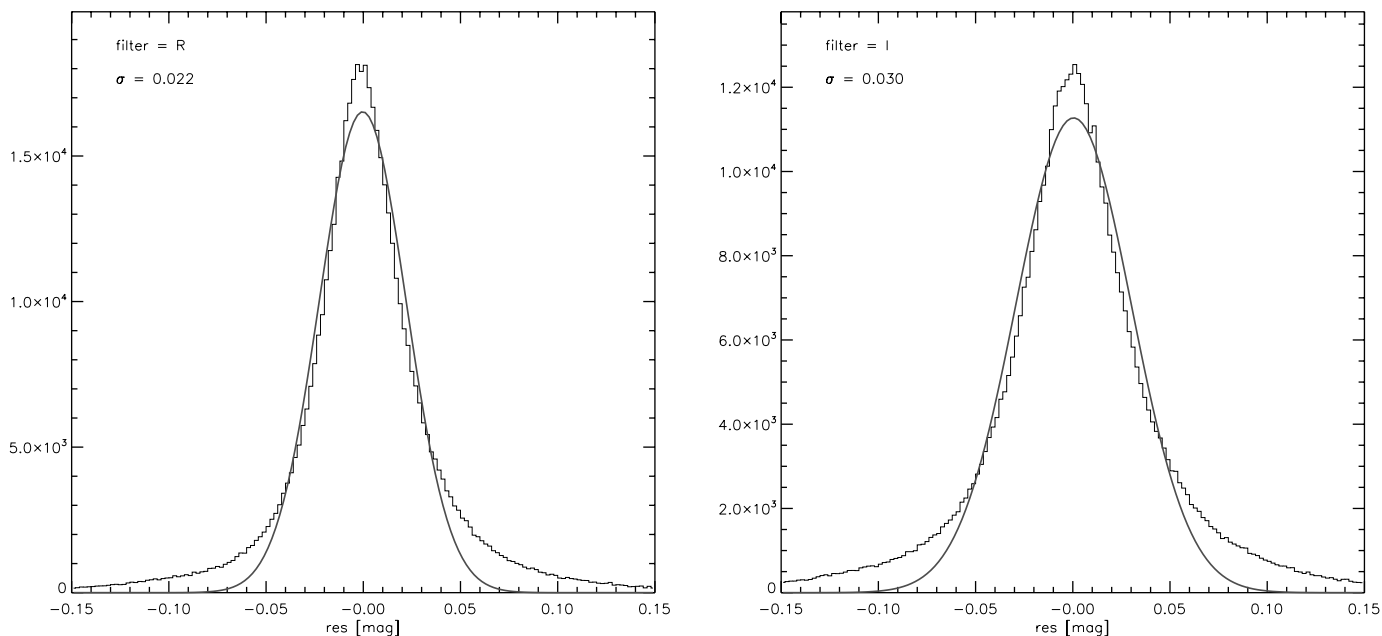$$R_{\mathrm{CTIO}} = R_{\mathrm{Landolt}} + k_{RI}^{R}(R_{\mathrm{Landolt}} - I_{\mathrm{Landolt}}) \tag{8}$$

Fig. 8.—Distribution of the night-to-night photometric residuals in magnitudes for CTIO 4 m R-band (*left*) and I-band (*right*) measurements of ESSENCE field stars. The solid lines are Gaussians fitted to the data. The small widths of the histograms ($\sim$2%–3%) demonstrate the temporal stability of our photometry. [*See the electronic edition of the Journal for a color version of this figure.*]

and

$$I_{\mathrm{CTIO}} = I_{\mathrm{Landolt}} + k_{RI}^{I}(R_{\mathrm{Landolt}} - I_{\mathrm{Landolt}}). \qquad (9)$$

Thus, we choose to adopt the same zero point for R_{CTIO}, I_{CTIO} for stars of zero color in the Landolt system. The color terms k_{RI}^{R}, k_{RI}^{I} may then be measured by comparing Landolt standard magnitudes with MOSAIC instrumental magnitudes.

We obtain the values $k_{RI}^{R} = -0.030$ and $k_{RI}^{I} = 0.030$ by combining our own work with the information reported on the CTIO 4 m Web site[25] and with synthetic photometry using 4 m MOSAIC passbands and the Stritzinger et al. (2006) spectrophotometric standards. These were also cross-checked by combining aperture-corrected DoPHOT magnitudes and 0.9 m catalogs.

This 0.9 m photometry, now transformed to the CTIO MOSAIC natural photometric system, was used to compute the zero points of the two subfields covered by the 0.9 m field of view for each of the ESSENCE fields. To generate catalogs for the other subfields, we must propagate the photometric zero point from these subfields across the rest of the MOSAIC. This requires that the instrumental sensitivities are normalized to a common level, such that one data unit corresponds to the same amount of incident flux for every subfield, and that we measure the *same* fraction of the flux for the stars in all the images, which can be achieved by correcting the PSF magnitudes to an aperture that encloses the total flux. If these two conditions are met, then the zero point derived for one subfield is valid for the entire MOSAIC.

To ensure that the sensitivities are normalized from subfield to subfield, we use the ratios of the sky levels between subfields, for all the images for a given night, to establish these relative flux scalings. Because of the enormous numbers of pixels used to measure this ratio, the results are incredibly precise and the normalization factors can be measured to $\sim$0.3%. This method actually normalizes the CCD sensitivities for the spectral energy distribution of the sky, which obviously differs from those of astronomical objects we seek to measure. However, tests using a range of

passband sensitivity curves and a variety of input spectra show that the resulting photometric errors are much less than 1%. Although the method is unaffected by uniform variations in sky brightness across the entire MOSAIC, care must be taken to avoid applying this method in the presence of moonlight, which could result in a systematic gradient in sky brightness across the array.

We then turn to the photometry of stars in the ESSENCE fields, which have been measured using DoPHOT PSF photometry. To correct these magnitudes so that they measure the total flux for the objects in the images, we use the standard method from aperture photometry of constructing a "growth curve" for each image from the incremental flux in concentric annuli around the objects. We choose a small aperture, for which we robustly determine the offset between the PSF magnitudes and aperture magnitudes for the brightest stars in the image. We then construct a growth curve out to an aperture at sufficiently large radius that the flux measured at those annuli is consistent with zero. Such aperture corrections are calculated for each subfield image in a field and are then used to bring all of the PSF photometry onto the same flux scale. Note that while the PSF does vary across the field of view of the MOSAIC, the small number of isolated stars in a typical ESSENCE field makes robust determination of spatially varying aperture corrections difficult, so instead a single correction is calculated for each subfield image.

With the photometry of the stars in all subfields now on the same flux scale, we are able to propagate photometric zero points across the whole MOSAIC. In this manner, we calibrate magnitudes for all the stars present in our fields for several epochs and then compute σ-clipped averages over all of the measurements. Figure 8 demonstrates that there is a small dispersion in the residuals about the mean for all the stars in our catalogs. This shows that the zero-point propagation procedure is robust from night to night.

To check the field-to-field consistency of these catalogs, we consider the ESSENCE data taken under photometric conditions. For a given night, we correct the zero points for each by applying aperture and air-mass corrections. We then take the average value of those corrected zero points as the true zero point for the entire night.
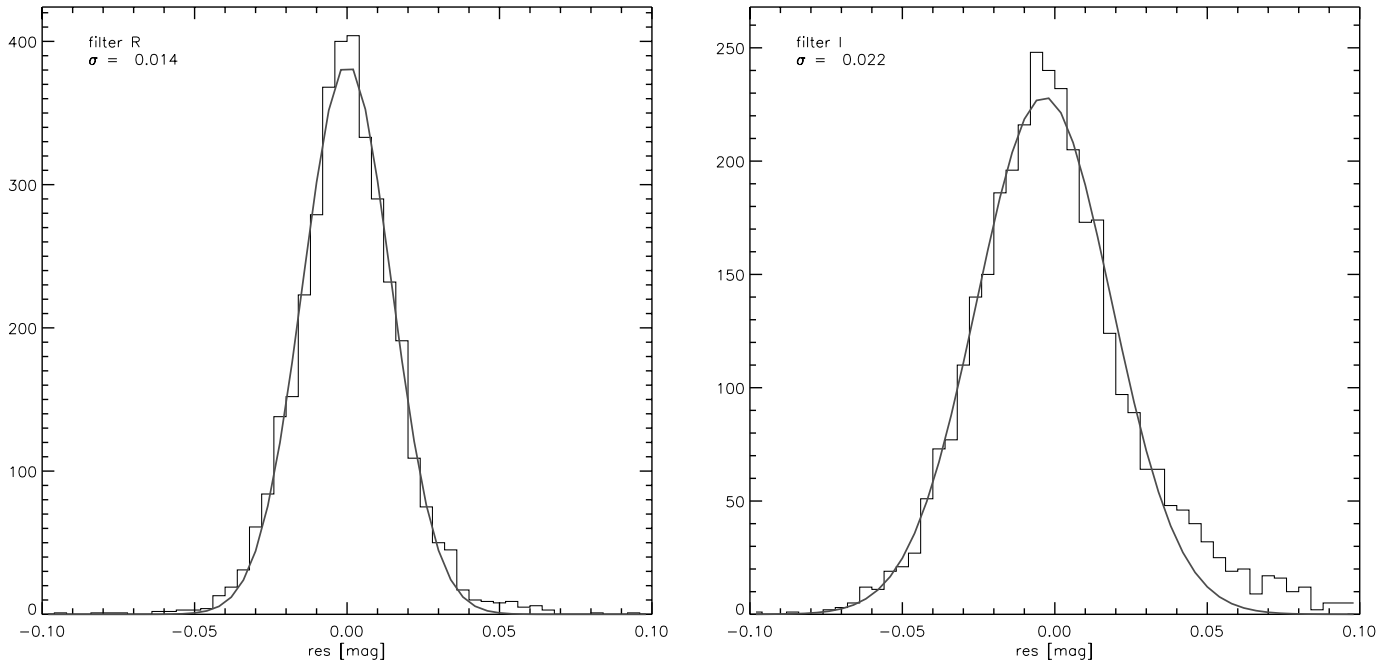
Fɪɢ. 9.—Distribution of photometric zero-point residuals, in magnitudes, for the *R* band (*left*) and the *I* band (*right*). The small scatter of ∼1%–2% demonstrates that our zero points are homogeneous across the ESSENCE fields. The solid lines are Gaussians fitted to the data. [*See the electronic edition of the Journal for a color version of this figure.*]

We then also calibrate each field individually, using our photometric catalogs. In Figure 9 we show the distribution of the differences between the zero points calculated using the ESSENCE catalogs and the average nightly zero point. The small scatter of 0.02 mag in each passband assures us that the zero points are consistent from field to field with a precision of better than 2%.

4.4. *Supernova Flux Measurement*

With accurately determined fluxes of the stars in our fields in the natural system, we then seek to measure the supernova fluxes as accurately as possible. This requires that we remove the background light due to the host galaxy, via image subtraction using the same software as in the search pipeline (§ 2.2.5). It is crucial that the subtraction procedure maintains the flux scaling from the original image, which has been calibrated to stars, through to the subtracted image, where we measure the supernova flux.

To test whether the image registration and subtraction stages affect our photometry, we added thousands of synthetic stars in a subsample of our images before these steps. These synthetic stars are generated using the DoPHOT analytic model for PSF, using typical shape parameters for the ESSENCE data and with appropriate statistical noise added. The flux of those stars was then measured after image registration and after template subtraction, respectively. The results are shown in Figures 10 and 11. We find that image registration and subtraction do not significantly bias our photometry, although the nominal photometric uncertainty from our noise maps slightly underestimates the true photometric uncertainty. Accordingly, the photometric uncertainty in the photometry presented here has been scaled up by an additional 20%.

To further study the uncertainties in our photometry as estimated using the noise maps, we measure fluxes using the DoPHOT PSF in a regular grid across the difference image, where there are no sources of flux. If the nominal photometric uncertainty were accurate, then we should find that the distribution of flux/σ_{flux} measured with the PSF in these empty regions should be centered

on zero with $\sigma = 1.0$. In practice, we find that this distribution is somewhat broader ($\sigma \approx 1.2$) for a typical difference image. We interpret this to mean that our uncertainties are slightly underestimated, probably due to pixel-to-pixel covariances generated in the remapping and convolution steps that are not accounted for
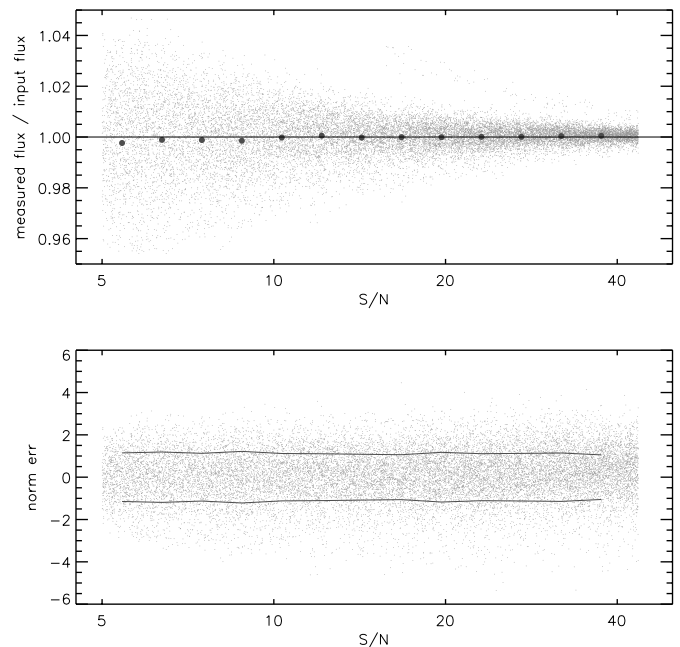
Fɪɢ. 10.—Fake stars were added to images before remapping, which rebins pixels. The top panel shows the ratio of the flux measured to the input flux in the rebinned image, as a function of the S/N of the fake star. Light gray points are individual stars, dark gray points are averages. Rebinning does not significantly bias our photometry, even at low S/N. The bottom panel shows the ratio of the flux residuals (input flux minus measured flux) divided by the estimated error using our noise maps, as a function of S/N. The solid lines denote one standard deviation. We find that the distribution is slightly broader than expected ($\sigma = 1.1$), indicating that our nominal uncertainty computed using the noise maps slightly underestimates the actual uncertainty by 10%. [*See the electronic edition of the Journal for a color version of this figure.*]
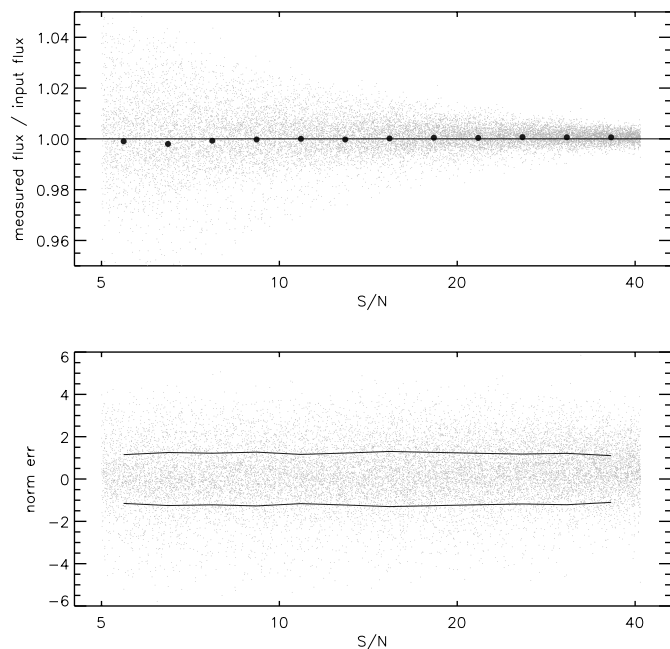
Fig. 11.—Same as Fig. 10, except the fake stars have been remeasured after template subtraction. The photometry remains linear to much better than 1%, even at low S/N. The normalized error distribution has $\sigma = 1.2$, so we scale the photometric uncertainty of measurements on subtracted images up by 20% from the value obtained from the noise maps. [*See the electronic edition of the Journal for a color version of this figure.*]

Fig. 12.—Ratio of recovered to input flux due to systematic misalignment of the PSF for the typical centroiding error as a function of the cumulative S/N of the object over all photometric measurements. By combining all measurements in both passbands, the positions of even faint SNe are constrained at a level corresponding to S/N > 10. [*See the electronic edition of the Journal for a color version of this figure.*]

properly in the noise maps. We scale up the photometric uncertainties for each difference image by a factor of 1.2.

On each difference frame, the PSF used to measure the supernova is determined using field stars prior to subtraction. For each subtraction, we convolve the image with the narrower PSF to match the broader PSF in the other image; it is this broader PSF that is used to measure the supernova in the difference image. The flux calibration of that same image, from comparing DoPHOT photometry to the catalogs described in § 4.1, is scaled by the normalization of the subtraction kernel and then applied to the supernova flux measured in the difference image.

To measure the supernova flux accurately, we fix the PSF to the best measured location of the supernova, rather than allow the position to be a free parameter in the PSF fit. Because fitting the PSF at a position displaced from the true source center would result in a systematic underestimate of the measured flux for the entire light curve, we estimate the size of this effect for our typical positional errors. The location for each supernova is refined from its discovery position by taking the average of all detections with an S/N of 5 or greater in all the available difference image frames. These derived positions are accurate to within 0.02″ within our astrometric system. In Figure 12 such a systematic is quantified by artificially shifting sources of known flux that have an FWHM of 1.0″, the average value for the ESSENCE survey. Our SN light curves are usually very well sampled, providing a cumulative S/N greater than 10 even for the highest redshift objects. This effective S/N translates to a photometric uncertainty less than 1.0%.

To obtain an optimal S/N in our subtractions, we make use of all of the images that contain background galaxy light. We follow the "NN2 methodology" outlined in Barris et al. (2005), which utilizes the flux differences from all $N(N-1)/2$ possible image pairs to estimate the supernova flux.

When dealing with the thousands of difference images generated in our NN2 method, automated and quantitative quality

controls were crucial for extracting good measurements. A second check was to measure the flux of known stars in the difference image. Ideally, there should be no excess of positive or negative flux in the difference image if the subtraction process was successful. After sigma clipping to reject variable stars, the average flux/σ_{flux} at the positions of all the stars was measured, and if it was inconsistent with the flux uncertainty expected for the difference image, that difference image was not used to measure the supernova flux. Once the quality-controlled full sets of $N(N-1)/2$ data files were generated, they were run through the NN2 program of Barris et al. (2005) to generate our final supernova light curves included in this paper.

5. PHOTOMETRY FROM THE ESSENCE FOUR-YEAR SAMPLE

We present here four sample ESSENCE light curves to illustrate the quality of the ESSENCE photometry (Fig. 13). These objects were chosen to be closest in redshift to an arbitrary set of redshifts ($z = 0.20, 0.35, 0.50,$ and 0.65) that span the range of the ESSENCE redshift distribution. For the purposes of plotting, all data from the season in which the SN was discovered are displayed. Photometry is presented in linear flux units in the CTIO 4 m natural system, where the formula for conversion to standard magnitudes is

$$m = -2.5 \log \mathcal{F} + 25. \qquad (10)$$

The full set of ESSENCE light curves and system throughput curves is available online.[26]

Since the photometry is reported in the CTIO 4 m natural system, the system throughput curves are an integral part of the

---

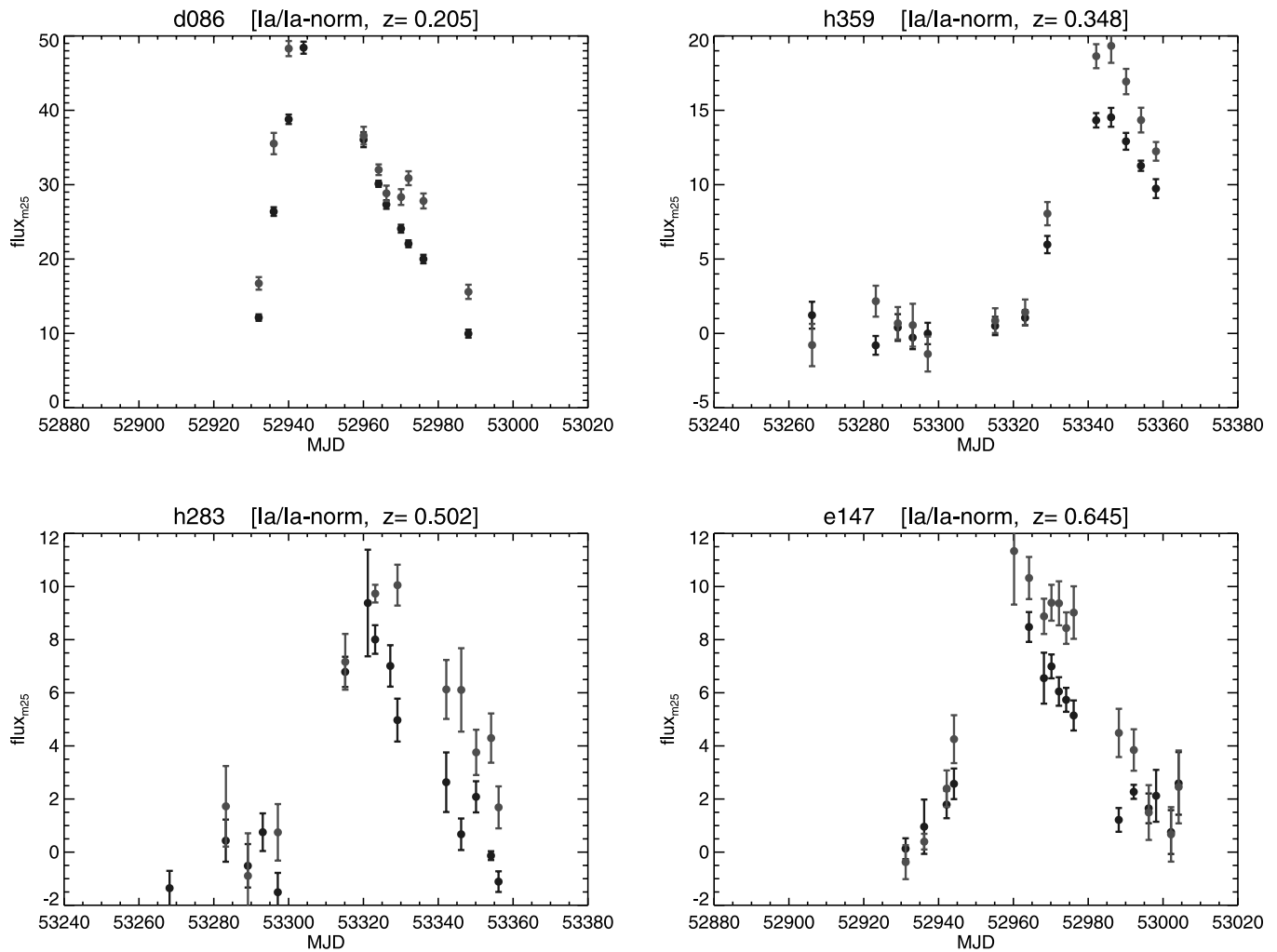[26] See http://www.ctio.noao.edu/essence/.

Fig. 13.— Example ESSENCE light curves, in units of linear flux, scaled such that flux = 1 corresponds to magnitude 25 (*dark gray*: *R*; *light gray*: *I*). Only data from the observing season in which the object was discovered are plotted. [*See the electronic edition of the Journal for a color version of this figure.*]
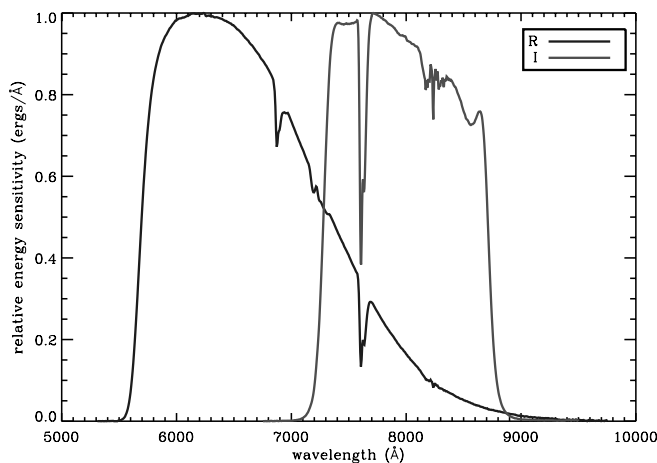

Fig. 14.— Throughput curves for the CTIO 4 m *R* and *I* bandpasses. These represent the full system throughput, which includes the wavelength dependence of the CCD quantum efficiency, the optical filters, the aluminum reflectance for the mirrors in the 4 m telescope, and a model for the typical atmosphere transmissivity. The curves here are represented in relative energy sensitivity in ergs Å^{-1}. Each curve has been normalized to unity at its peak. [*See the electronic edition of the Journal for a color version of this figure.*]

data set and are presented here as well (Fig. 14). These system throughput curves are the product of the following:

1. The CTIO MOSAIC *R* and *I* filters, as measured in the laboratory.
2. Standard quantum efficiency curves for the CCDs from the manufacturer (Tek).
3. The wavelength dependence of aluminum, for the two surfaces in the 4 m telescope.
4. Typical atmospheric transmission, with losses due to scattering and molecular absorption, calculated from taking the observations of spectrophotometric standards[27] with removal of the telluric features (Bessell 1999) to determine the average atmospheric absorption at CTIO.

We are also developing a novel technique for measuring the full wavelength-dependent response of the telescope/camera system through the use of a tunable laser and a calibrated photodiode (Stubbs & Tonry 2006). Preliminary results from this new method are consistent with the estimates we derived from the product of each component as described above (Stubbs et al. 2007).

6. CONCLUSIONS

We have presented the scientific motivation for the ESSENCE survey, which aims to constrain the equation-of-state parameter

---

[27] Vizier Online Data Catalog, II/179 (M. Hamuy et al., 1995).

of dark energy, w, to 10%. Modeling our survey suggests that there is a slight gain in the accuracy of measuring w by covering a greater volume at lower redshifts by pushing the survey to relatively short exposure times. We describe how, using the survey strategy and software outlined here, we detect likely high-redshift supernovae using rapid analysis of survey data and how we analyze spectra to confidently identify objects as SNe Ia and measure their redshifts. The photometry for these 102 SNe Ia is presented here, in the CTIO 4 m natural system, as detailed in this paper.

Once we have identified the sample of good SNe Ia and carefully measured their light curves, the next step is to estimate distances to these objects. A detailed description of the process of turning supernova photometry and redshifts to cosmological distances and, finally, to constraints on cosmological parameters follows in a companion paper (Wood-Vasey et al. 2007).

ESSENCE has two remaining years of operation. In addition to increasing the sample size, we are undertaking a focused effort to improve the photometric calibration of the CTIO 4 m telescope and thus reduce the potential systematic errors from miscalibration. This program has been awarded nine nights of engineering time specifically for the goal of improving the MOSAIC calibrations via concentrated observations of standard-star fields, along with fields observed by ESSENCE and other ongoing CTIO 4 m surveys. With a final sample of $\sim$150 SNe Ia and an improvement in photometric precision from the current 2% to a final 1%, we will reach the goal of the project: a measurement of w to 10%.

REFERENCES

Alard, C. 2000, A&AS, 144, 363
Alard, C., & Lupton, R. H. 1998, ApJ, 503, 325
Albrecht, A., et al. 2006, preprint (astro-ph/0609591)
Appenzeller, I., et al. 1998, Messenger, 94, 1
Astier, P., et al. 2006, A&A, 447, 31
Barris, B. J., Tonry, J. L., Novicki, M. C., & Wood-Vasey, W. M. 2005, AJ, 130, 2272
Barris, B. J., et al. 2004, ApJ, 602, 571
Benetti, S., Cappellaro, E., Turatto, M., Taubenberger, S., Harutyunyan, A., & Valenti, S. 2006, ApJ, 653, L129
Bertin, E., Mellier, Y., Radovich, M., Missonnier, G., Didelon, P., & Morin, B. 2002, in ASP Conf. Ser. 281, Astronomical Data Analysis Software and Systems XI, ed. D. A. Bohlender, D. Durand, & T. H. Handley (San Francisco: ASP), 228
Bessell, M. S. 1999, PASP, 111, 1426
Bessell, M. S., Castelli, F., & Plez, B. 1998, A&A, 333, 231
Blondin, S., & Tonry, J. 2007, ApJ, in press
Blondin, S., Walsh, J. R., Leibundgut, B., & Sainton, G. 2005, A&A, 431, 757
Bohlin, R. C. 2007, in ASP Conf. Ser. 364, The Future of Photometric, Spectrophotometric and Polarimetric Standardization, ed. C. Sterken (San Francisco: ASP), 315
Bohlin, R. C., & Gilliland, R. L. 2004, AJ, 127, 3508
Branch, D., Livio, M., Yungelson, L. R., Boffi, F. R., & Baron, E. 1995, PASP, 107, 1019
Candia, P., et al. 2003, PASP, 115, 277
Carroll, S. M., Press, W. H., & Turner, E. L. 1992, ARA&A, 30, 499
Clocchiatti, A., et al. 2006, ApJ, 642, 1
Colgate, S. A., & McKee, C. 1969, ApJ, 157, 623
Conley, A., et al. 2006, AJ, 132, 1707
Contardo, G., Leibundgut, B., & Vacca, W. D. 2000, A&A, 359, 876
Copeland, E. J., Sami, M., & Tsujikawa, S. 2006, Int. J. Mod. Phys. D, 15, 1753
Dressler, A. 2004, A User's Manual for IMACS
Dvali, G., Gabadadze, G., & Shifman, M. 2003, Phys. Rev. D, 67, 044020
Eisenstein, D. J., et al. 2005, ApJ, 633, 560
Faber, S. M., et al. 2003, Proc. SPIE, 4841, 1657
Fabricant, D., Cheimets, P., Caldwell, N., & Geary, J. 1998, PASP, 110, 79
Filippenko, A. V. 1997, ARA&A, 35, 309
Filippenko, A. V., Matheson, T., & Ho, L. C. 1993, ApJ, 415, L103
Filippenko, A. V., et al. 1992a, AJ, 104, 1543
———. 1992b, ApJ, 384, L15
Freedman, W. L., & Turner, M. S. 2003, Rev. Mod. Phys., 75, 1433
Frieman, J., et al. 2004, BAAS, 36, 1548
Gallagher, J. S., Garnavich, P. M., Berlind, P., Challis, P., Jha, S., & Kirshner, R. P. 2005, ApJ, 634, 210

Garg, A., et al. 2007, AJ, 133, 403
Garnavich, P. M., et al. 1998, ApJ, 509, 74
Goldhaber, G., et al. 2001, ApJ, 558, 359
Guy, J., Astier, P., Nobili, S., Regnault, N., & Pain, R. 2005, A&A, 443, 781
Hamuy, M., Phillips, M. M., Suntzeff, N. B., Schommer, R. A., Maza, J., & Aviles, R. 1996, AJ, 112, 2398
Hamuy, M., Trager, S. C., Pinto, P. A., Phillips, M. M., Schommer, R. A., Ivanov, V., & Suntzeff, N. B. 2000, AJ, 120, 1479
Hamuy, M., et al. 1993, AJ, 106, 2392
———. 2003, Nature, 424, 651
Hatano, K., Branch, D., & Deaton, J. 1998, ApJ, 502, 177
Hillebrandt, W., & Niemeyer, J. C. 2000, ARA&A, 38, 191
Hook, I., et al. 2003, Proc. SPIE, 4841, 1645
Horne, K. 1986, PASP, 98, 609
Hoyle, F., & Fowler, W. A. 1960, ApJ, 132, 565
Jha, S. 2002, Ph.D. thesis, Harvard Univ.
Jha, S., Riess, A. G., & Kirshner, R. P. 2007, ApJ, 659, 122
Jha, S., et al. 2006, AJ, 131, 527
Knop, R. A., et al. 2003, ApJ, 598, 102
Krisciunas, K., et al. 2005, AJ, 130, 2453
Landolt, A. U. 1983, AJ, 88, 439
———. 1992, AJ, 104, 340
Li, W., Filippenko, A. V., & Riess, A. G. 2001a, ApJ, 546, 719
Li, W., et al. 2001b, PASP, 113, 1178
———. 2003, PASP, 115, 453
Livio, M. 2000, in Type Ia Supernovae, Theory and Cosmology, ed. J. C. Niemeyer & J. W. Truran (Cambridge: Cambridge Univ. Press), 33
Matheson, T., Filippenko, A. V., Ho, L. C., Barth, A. J., & Leonard, D. C. 2000a, AJ, 120, 1499
Matheson, T., et al. 2000b, AJ, 120, 1487
———. 2005, AJ, 129, 2352
Mulchaey, J. 2001, LDSS-2 User's Guide
Nomoto, K., Umeda, H., Kobayashi, C., Hachisu, I., Kato, M., & Tsujimoto, T. 2000, in AIP Conf. Proc. 522, Cosmic Explosions: Tenth Astrophysics Conference, ed. S. S. Holt & W. W. Zhang (Melville: AIP), 35
Norgaard-Nielsen, H. U., Hansen, L., Jorgensen, H. E., Aragon Salamanca, A., & Ellis, R. S. 1989, Nature, 339, 523
Nugent, P., Kim, A., & Perlmutter, S. 2002, PASP, 114, 803
Oke, J. B., et al. 1995, PASP, 107, 375
Padmanabhan, T. 2003, Phys. Rep., 380, 235
Peebles, P. J., & Ratra, B. 2003, Rev. Mod. Phys., 75, 559

Perlmutter, S., et al. 1995, ApJ, 440, L41
———. 1999, ApJ, 517, 565
Phillips, M. M. 1993, ApJ, 413, L105
Prieto, J. L., Rest, A., & Suntzeff, N. B. 2006, ApJ, 647, 501
Renzini, A. 1996, in IAU Colloq. 145, Supernovae and Supernova Remnants, ed. R. McCray & Z. Wang (Cambridge: Cambridge Univ. Press), 77
Riess, A. G., Press, W. H., & Kirshner, R. P. 1996, ApJ, 473, 88
Riess, A. G., et al. 1998, AJ, 116, 1009
———. 1999a, AJ, 117, 707
———. 1999b, AJ, 118, 2675
———. 2001, ApJ, 560, 49
———. 2004, ApJ, 607, 665
———. 2007, ApJ, 659, 98
Schechter, P. L., Mateo, M., & Saha, A. 1993, PASP, 105, 1342
Schmidt, B. P., et al. 1998, ApJ, 507, 46
Schmidt, G. D., Weymann, R. J., & Foltz, C. B. 1989, PASP, 101, 713
Sheinis, A. I., Bolte, M., Epps, H. W., Kibrick, R. I., Miller, J. S., Radovan, M. V., Bigelow, B. C., & Sutin, B. M. 2002, PASP, 114, 851
Spergel, D. N., et al. 2007, ApJS, 170, 377
Steinhardt, P. J. 2003, Philos. Trans. R. Soc. London A, 361, 2497
Steinhardt, P. J., & Turok, N. 2002, Science, 296, 1436
———. 2005, NewA Rev., 49, 43
Stritzinger, M., Leibundgut, B., Walch, S., & Contardo, G. 2006, A&A, 450, 241
Stubbs, C. W., & Tonry, J. L. 2006, ApJ, 646, 1436
Stubbs, C. W., et al. 2007, in ASP Conf. Ser. 364, The Future of Photometric, Spectrophotometric and Polarimetric Standardization, ed. C. Sterken (San Francisco: ASP), 373
Sullivan, M., et al. 2006, ApJ, 648, 868
Tegmark, M., et al. 2004, Phys. Rev. D, 69, 103501
Tonry, J., & Davis, M. 1979, AJ, 84, 1511
Tonry, J. L., et al. 2003, ApJ, 594, 1
Upadhye, A., Ishak, M., & Steinhardt, P. J. 2005, Phys. Rev. D, 72, 063501
Wade, R. A., & Horne, K. 1988, ApJ, 324, 411
Weinberg, S. 1989, Rev. Mod. Phys., 61, 1
Weller, J., & Albrecht, A. 2002, Phys. Rev. D, 65, 103512
Wood-Vasey, W. M., Wang, L., & Aldering, G. 2004, ApJ, 616, 339
Wood-Vasey, W. M., et al. 2007, ApJ, 666, 694
Woosley, S. E., & Weaver, T. A. 1986, ARA&A, 24, 205
York, D. G., et al. 2000, AJ, 120, 1579
Zacharias, N., Urban, S. E., Zacharias, M. I., Wycoff, G. L., Hall, D. M., Monet, D. G., & Rafferty, T. J. 2004, AJ, 127, 3043